The Astrophysical Journal Letters, 963:L31 (23pp), 2024 March 1 https://doi.org/10.3847/2041-8213/ad27d4

On the Magnetic Field Properties of Protostellar Envelopes in Orion

Bo Huang (黄博)[1], Josep M. Girart[1,2], Ian W. Stephens[3], Manuel Fernández López[4], Hector G. Arce[5], John M. Carpenter[6], Paulo Cortes[7,8], Erin G. Cox[9], Rachel Friesen[10], Valentin J. M. Le Gouellec[11,28], Charles L. H. Hull[6,12], Nicole Karnath[13,14,15], Woojin Kwon[16,17], Zhi-Yun Li[18], Leslie W. Looney[19], S. Thomas Megeath[20], Philip C. Myers[15], Nadia M. Murillo[21,22], Jaime E. Pineda[23], Sarah Sadavoy[24], Álvaro Sánchez-Monge[1,2], Patricio Sanhueza[25,26], John J. Tobin[7], Qizhou Zhang[15], James M. Jackson[7], and Dominique Segura-Cox[23,27]

[1] Institut de Ciències de l'Espai (ICE-CSIC), Campus UAB, Can Magrans S/N, E-08193 Cerdanyola del Vallès, Catalonia, Spain; huang@ice.csic.es, girart@ieec.cat
[2] Institut d'Estudis Espacials de Catalunya (IEEC), c/Gran Capita, 2-4, E-08034 Barcelona, Catalonia, Spain
[3] Department of Earth, Environment, and Physics, Worcester State University, Worcester, MA 01602, USA
[4] Instituto Argentino de Radioastronomía (CCT-La Plata, CONICET; CICPBA), C.C. No. 5, 1894, Villa Elisa, Buenos Aires, Argentina
[5] Department of Astronomy, Yale University, New Haven, CT 06511, USA
[6] Joint ALMA Observatory, Av. Alonso de Córdova 3107, Vitacura, Santiago, Chile
[7] National Radio Astronomy Observatory, 520 Edgemont Rd., Charlottesville, VA 22093, USA
[8] Joint ALMA Observatory, Alonso de Córdova 3107, Vitacura, Santiago, Chile
[9] Center for Interdisciplinary Exploration and Research in Astrophysics (CIERA), 1800 Sherman Avenue, Evanston, IL 60201, USA
[10] Department of Astronomy & Astrophysics, University of Toronto, 50 St. George St., Toronto, ON M5S 3H4, Canada
[11] NASA Ames Research Center, Space Science and Astrobiology Division M.S. 245-6 Moffett Field, CA 94035, USA
[12] National Astronomical Observatory of Japan, Alonso de Córdova 3788, Office 61B, Vitacura, Santiago, Chile
[13] SOFIA Science Center, Universities Space Research Association, NASA Ames Research Center, Moffett Field, CA 94035, USA
[14] Space Science Institute, 4765 Walnut St., Suite B Boulder, CO 80301, USA
[15] Center for Astrophysics| Harvard & Smithsonian, 60 Garden Street, Cambridge, MA 02138, USA
[16] Department of Earth Science Education, Seoul National University, 1 Gwanak-ro, Gwanak-gu, Seoul 08826, Republic of Korea
[17] SNU Astronomy Research Center, Seoul National University, 1 Gwanak-ro, Gwanak-gu, Seoul 08826, Republic of Korea
[18] Astronomy Department, University of Virginia, Charlottesville, VA 22904, USA
[19] Department of Astronomy, University of Illinois, 1002 West Green Street, Urbana, IL 61801, USA
[20] Department of Physics and Astronomy, University of Toledo, Toledo, OH 43606, USA
[21] Instituto de Astronomía, Universidad Nacional Autónoma de México, AP106, Ensenada CP 22830, B.C., México
[22] Star and Planet Formation Laboratory, RIKEN Cluster for Pioneering Research, Wako, Saitama 351-0198, Japan
[23] Center for Astrochemical Studies, Max Planck Institute for Extraterrestrial Physics, D-85748 Garching, Germany
[24] Department of Physics, Engineering and Astronomy, Queen's University, 64 Bader Lane, Kingston, ON K7L 3N6, Canada
[25] National Astronomical Observatory of Japan, 2-21-1 Osawa, Mitaka, Tokyo 181-8588, Japan
[26] Astronomical Science Program, The Graduate University for Advanced Studies, SOKENDAI, 2-21-1 Osawa, Mitaka, Tokyo 181-8588, Japan
[27] Department of Astronomy, University of Texas, 2515 Speedway, Stop C1400, Austin, TX 78712, USA
Received 2023 November 6; revised 2024 February 8; accepted 2024 February 9; published 2024 February 29

Abstract

We present 870 μm polarimetric observations toward 61 protostars in the Orion molecular clouds with $\sim$400 au (1″) resolution using the Atacama Large Millimeter/submillimeter Array. We successfully detect dust polarization and outflow emission in 56 protostars; in 16 of them the polarization is likely produced by self-scattering. Self-scattering signatures are seen in several Class 0 sources, suggesting that grain growth appears to be significant in disks at earlier protostellar phases. For the rest of the protostars, the dust polarization traces the magnetic field, whose morphology can be approximately classified into three categories: standard-hourglass, rotated-hourglass (with its axis perpendicular to outflow), and spiral-like morphology. A total of 40.0% ($\pm$3.0%) of the protostars exhibit a mean magnetic field direction approximately perpendicular to the outflow on several $\times$ 10^2–10^3 au scales. However, in the remaining sample, this relative orientation appears to be random, probably due to the complex set of morphologies observed. Furthermore, we classify the protostars into three types based on the $C^{17}O$ (3–2) velocity envelope's gradient: perpendicular to outflow, nonperpendicular to outflow, and unresolved gradient ($\lesssim$1.0 km s^{-1} arcsec^{-1}). In protostars with a velocity gradient perpendicular to outflow, the magnetic field lines are preferentially perpendicular to outflow, with most of them exhibiting a rotated hourglass morphology, suggesting that the magnetic field has been overwhelmed by gravity and angular momentum. Spiral-like magnetic fields are associated with envelopes having large velocity gradients, indicating that the rotation motions are strong enough to twist the field lines. All of the protostars with a standard-hourglass field morphology show no significant velocity gradient due to the strong magnetic braking.

Unified Astronomy Thesaurus concepts: Star formation (1569); Magnetic fields (994); Protostars (1302)

1. Introduction

Magnetic fields (henceforth *B*-fields) are thought to play a crucial role in the star-forming processes (e.g., Maury et al. 2022; Pattle et al. 2023). In ideal MHD models, during the collapse phase of a prestellar core, the *B*-field lines are drawn

[28] NASA Postdoctoral Program Fellow.

inward into an hourglass morphology, forming a pseudo-disk. They carry away angular momentum very efficiently, which ultimately leads to catastrophic magnetic braking, preventing the formation of a centrifugally supported disk (Ciolek & Mouschovias 1994; Allen et al. 2003; Galli et al. 2006). In real astrophysical environments, various nonideal MHD effects may come into play, allowing the formation of an accretion disk around the central protostar (Dapp & Basu 2010; Hennebelle et al. 2016, 2020; Zhao et al. 2020). In addition, an initial misalignment between the *B*-field and the rotation axis leads to weaker magnetic braking of the collapsing core, enabling early disk formation (e.g., Joos et al. 2012; Li et al. 2013; Hirano & Machida 2019; Machida et al. 2020). In any case, *B*-fields are also thought to be important in the formation, collimation, acceleration, and regulation of outflows associated with protostellar systems (e.g., Pudritz & Ray 2019).

Polarized dust continuum emission allows us to examine the *B*-field morphology in star-forming regions. In the presence of *B*-fields, spinning and elongated dust grains with paramagnetic properties are expected to align their long axes perpendicular to the field direction (e.g., Hoang & Lazarian 2009; Andersson et al. 2015). In recent decades, dust polarization observations carried out with (sub)millimeter interferometers have increasingly demonstrated their effectiveness in mapping *B*-fields at the scales of cores ($\sim 10^4$ au) and envelopes ($\sim 10^2$–10^4 au; e.g., Girart et al. 1999, 2013; Cox et al. 2018; Galametz et al. 2018; Hull & Zhang 2019; Le Gouellec et al. 2020; Cortés et al. 2021). Hourglass-shaped *B*-fields have been observed around protostellar envelopes and trace gravitationally infalling material (e.g., Girart et al. 2006, 2009; Qiu et al. 2014; Beltrán et al. 2019; Le Gouellec et al. 2019; Hull et al. 2020). Building on these observations, some studies developed 3D analytical models of hourglass morphology (e.g., Myers et al. 2018, 2020), further reinforcing the prevalence of this structure. However, interferometric polarization surveys toward low- and high-mass protostars at core and envelope scales found that the *B*-field does not correlate with the axis of outflows. This suggests that the *B*-field may be less dynamically important than angular momentum and gravity (Hull et al. 2013; Zhang et al. 2014).

On the other hand, millimeter polarized emission in planet-forming disks is dominated by self-scattering of large dust grains (∼several hundred microns; Kataoka et al. 2015, 2016; Yang et al. 2016a, 2016b). Recent high-resolution observations of dust polarization have revealed polarization patterns that more closely align with self-scattering, rather than the signature expected from *B*-fields within protostellar and protoplanetary disks (Stephens et al. 2017b; Kataoka et al. 2017; Sadavoy et al. 2018a; Bacciotti et al. 2018; Cox et al. 2018; Girart et al. 2018; Hull et al. 2018; Yang et al. 2019). Only a few observations show cases where the polarization is consistent with magnetically aligned dust grains on disk scales (Sadavoy et al. 2018b; Alves et al. 2018; Lee et al. 2018; Ohashi et al. 2018).

The Orion molecular clouds (OMCs) are one of the best regions to study the role of *B*-fields in the star formation process. They are the closest (∼400 pc; Kounkel et al. 2017) high-mass/intermediate-mass star-forming regions and have been extensively studied across multiple wavelengths, providing a wealth of ancillary data and information. Moreover, most solar-type stars, including the Sun, formed in massive, clustered star-forming regions (Lada & Lada 2003), making the OMCs a more typical representation of star-forming conditions within the Galaxy. Finally, the OMCs have the largest population of Class 0 protostars within 500 pc (Stutz et al. 2013; Furlan et al. 2016). Class 0 protostars are exceptionally well suited for studying the role of *B*-fields in star formation owing to their early evolutionary stage that preserves information about their initial collapse.

The *B*-field Orion Protostellar Survey (BOPS) used the Atacama Large Millimeter/submillimeter Array (ALMA) to observe 870 μm dust polarization toward 61 young, low-mass protostars in the OMCs. Its main objective is to investigate the role of *B*-fields on spatial scales ranging from 400 to thousands of au, fully encompassing the protostellar envelope surrounding the youngest protostars. The limited sensitivity of previous surveys (e.g., Hull et al. 2014; Zhang et al. 2014) probed sources at varying evolutionary stages and in different star-forming regions, thus resulting in samples that were biased and nonuniform. To mitigate this, the BOPS observations uniformly probe *B*-field structures within the envelopes surrounding protostars in one star-forming region. In this paper, we present the first results of the BOPS project, organized as follows: Section 2 introduces the observations and the processes of data reduction. The main results are presented in Section 3, followed by a detailed discussion of these results in Section 4. Finally, the summary is given in Section 5.

2. Observations and Data Reduction

The BOPS (PI: Ian Stephens, 2019.1.00086) survey used ALMA Band 7 (870 μm) to observe 57 fields, each centered on a different protostar as identified by the VLA/ALMA Nascent Disk and Multiplicity (VANDAM) Survey of Orion Protostars (Tobin et al. 2020). The vast majority of these protostars are Class 0, though a few bright Class I protostars were also included in the sample. The names and coordinates of these protostars are listed in Table 1. We targeted the brightest Class 0 sources using their Very Large Array, C-array, 9 mm fluxes ($\sim 1''$ resolution). The sample size was selected to be approximately twice that of the TADPOL survey (Hull et al. 2014), which included 30 sources throughout different star-forming regions. Observations were made from 2019 November 29 to 2019 December 20, using the ALMA compact configurations C43-1 and C43-2 and an intermediate configuration of both, which provided baselines between about 14 and 312 m. The observations were taken in frequency division mode (FDM), providing modest spectral resolutions. We used four spectral windows, two in each sideband, with the upper sideband targeting ^{12}CO (3–2) and continuum and the lower sideband targeting the continuum only. The maximum bandwidth (1.875 GHz per spectral window) was selected for the continuum, while a more modest bandwidth but higher spectral resolution were used for ^{12}CO (3–2). Notably, C^{17}O (3–2) in spectral window 4 was detected toward each protostar, which we used to trace the envelope kinematics. Other molecular transition lines were detected because of the resolution provided by the ALMA FDM mode but are not considered here. The rest frequency, bandwidth, spectral resolution, and velocity resolution of each spectral window are listed in Table 2.

Table 1
Source Properties for the Entire Sample

Name	R.A. (h:m:s)	Decl. (d:m:s)	Beam (arcsec × arcsec)	P.A. (deg)	D (pc)	Class	$L_{\rm bol}$ ($L_\odot$)	$T_{\rm bol}$ (K)	σ_I (mJy)	$\sigma_{^{12}{\rm CO}}$ (mJy)	$\sigma_{{\rm C}^{17}{\rm O}}$ (mJy)	Type Stokes I
HH212M	05:43:51.41	−01:02:53.25	0.95 × 0.70	−70.0	429.2	0	14.00	53.0	0.10	30.0	2.2	Extended
HH270IRS	05:51:22.72	02:56:04.95	0.93 × 0.71	−79.0	460.0	I	/	/	0.13	95.0	1.8	Compact
HOPS-10	05:35:09.05	−05:58:26.94	0.92 × 0.66	−68.8	388.2	0	3.33	46.2	0.09	25.0	2.7	Compact
HOPS-11	05:35:13.43	−05:57:57.96	0.90 × 0.66	−70.2	388.3	0	9.00	48.8	0.11	53.0	2.7	Compact
HOPS-12E	05:35:08.95	−05:55:55.04	0.82 × 0.66	−78.8	388.6	0	/	/	0.11	35.0	2.4	Binary
HOPS-12W	05:35:08.63	−05:55:54.70	0.92 × 0.66	−68.6	388.6	0	7.31	42.0	0.11	46.0	2.6	Binary
HOPS-50	05:34:40.92	−05:31:44.79	0.89 × 0.66	−70.3	391.5	0	4.20	51.4	0.08	14.0	2.4	Compact
HOPS-53	05:33:57.40	−05:23:30.05	0.82 × 0.66	−78.9	390.5	0	26.42	45.9	0.09	44.0	3.1	Extended
HOPS-60	05:35:23.29	−05:12:03.50	0.82 × 0.66	−79.1	392.8	0	21.93	54.1	0.12	79.0	2.3	Compact
HOPS-78	05:35:25.97	−05:05:43.43	0.82 × 0.66	−79.2	392.8	0	8.93	38.1	0.13	40.0	2.6	Extended
HOPS-81	05:35:28.02	−05:04:57.41	0.90 × 0.67	−69.6	392.8	0	1.24	40.1	0.08	41.0	1.7	Compact
HOPS-84	05:35:26.57	−05:03:55.20	0.91 × 0.66	−68.7	392.8	I	49.11	90.8	0.17	15.0	2.6	Compact
HOPS-87N	05:35:23.42	−05:01:30.62	0.82 × 0.66	−79.6	392.7	0	36.49	38.1	0.36	54.0	2.4	Binary
HOPS-87S	05:35:23.67	−05:01:40.32	0.82 × 0.66	−79.6	392.7	0	/	/	0.36	54.0	2.4	Binary
HOPS-88	05:35:22.47	−05:01:14.38	0.89 × 0.67	−70.9	392.7	0	15.81	42.4	0.18	119.0	2.2	Extended
HOPS-96	05:35:29.72	−04:58:48.68	0.82 × 0.66	−79.0	392.7	0	6.19	35.6	0.11	15.0	1.8	Compact
HOPS-124	05:39:19.91	−07:26:11.27	0.91 × 0.65	−69.5	398.0	0	58.29	44.8	0.37	59.0	3.0	Compact
HOPS-153	05:37:57.03	−07:06:56.32	0.89 × 0.66	−71.0	387.9	0	4.43	39.4	0.07	22.0	2.0	Extended
HOPS-164	05:37:00.43	−06:37:10.96	0.89 × 0.66	−70.6	385.0	0	0.58	50.0	0.07	36.0	2.1	Compact
HOPS-168	05:36:18.95	−06:45:23.63	0.81 × 0.66	−80.2	383.3	0	48.07	54.0	0.10	64.0	2.5	Extended
HOPS-169	05:36:36.17	−06:38:54.46	0.81 × 0.66	−80.1	384.0	0	3.91	32.5	0.10	49.0	2.1	Extended
HOPS-182	05:36:18.80	−06:22:10.29	0.82 × 0.66	−80.2	385.1	0	71.12	51.9	0.07	74.0	2.1	Extended
HOPS-203N	05:36:22.87	−06:46:06.68	0.82 × 0.66	−79.9	383.5	0	20.44	43.7	0.09	38.0	1.9	Multiple
HOPS-203S	05:36:22.90	−06:46:09.59	0.91 × 0.65	−69.3	383.5	0	/	/	0.12	36.0	2.6	Multiple
HOPS-224	05:41:32.07	−08:40:09.87	0.88 × 0.66	−70.9	440.3	0	2.99	48.6	0.09	36.0	2.0	Compact
HOPS-247	05:41:26.19	−07:56:51.95	0.88 × 0.66	−71.3	430.9	0	3.09	42.8	0.09	18.0	2.4	Compact
HOPS-250	05:40:48.85	−08:06:57.16	0.91 × 0.65	−69.7	428.5	0	6.79	69.4	0.10	74.0	2.5	Compact
HOPS-288	05:39:56.01	−07:30:27.67	0.81 × 0.66	−81.2	405.5	0	135.47	48.6	0.22	63.0	2.2	Extended
HOPS-303	05:42:02.65	−02:07:45.99	0.94 × 0.70	−71.4	410.0	0	1.49	43.2	0.10	19.0	2.6	Extended
HOPS-310	05:42:27.68	−01:20:01.40	0.93 × 0.69	−81.1	414.3	0	13.83	51.8	0.13	44.0	2.5	Compact
HOPS-317N	05:46:08.60	−00:10:38.54	0.94 × 0.69	−81.9	427.1	0	4.76	47.5	0.23	85.0	2.1	Binary
HOPS-317S	05:46:08.38	−00:10:43.64	0.94 × 0.69	−81.9	427.1	0	/	/	0.23	75.0	2.1	Binary
HOPS-325	05:46:39.20	00:01:12.25	0.96 × 0.70	−69.2	428.5	0	6.2	49.2	0.11	94.0	4.0	Extended
HOPS-340	05:47:01.32	00:26:23.00	0.96 × 0.70	−68.6	430.9	0	1.85	40.6	0.08	32.0	2.4	Binary
HOPS-341	05:47:00.92	00:26:21.45	0.96 × 0.70	−68.3	430.9	0	2.07	39.4	0.08	43.0	2.5	Binary
HOPS-354	05:54:24.27	01:44:19.82	0.93 × 0.70	−81.2	355.4	0	6.57	34.8	0.07	19.0	1.4	Extended
HOPS-358	05:46:07.26	−00:13:30.30	0.95 × 0.70	−70.2	426.8	0	24.96	41.7	0.13	44.0	2.6	Extended
HOPS-359	05:47:24.85	00:20:59.34	0.94 × 0.71	−70.8	429.4	0	10.00	36.7	0.13	8.0	1.8	Extended
HOPS-361N	05:47:04.64	00:21:47.77	0.94 × 0.69	−81.5	430.4	0	/	/	0.56	70.0	3.2	Binary
HOPS-361S	05:47:04.79	00:21:42.74	0.94 × 0.69	−81.8	430.4	0	478.99	69.0	1.15	130.0	3.0	Binary
HOPS-370	05:35:27.64	−05:09:34.45	0.91 × 0.66	−68.7	392.8	I	360.86	71.5	0.21	102.0	3.6	Extended
HOPS-373W	05:46:30.91	−00:02:35.20	0.95 × 0.70	−69.6	428.1	0	5.32	36.9	0.12	67.0	2.4	Binary
HOPS-373E	05:46:31.11	−00:02:33.10	0.95 × 0.70	−69.6	428.1	0	/	/	0.12	67.0	/	Binary
HOPS-383	05:35:29.79	−04:59:50.43	0.90 × 0.67	−69.9	392.8	0	7.83	45.8	0.07	28.0	2.0	Compact
HOPS-384	05:41:44.14	−01:54:46.05	0.93 × 0.69	−80.6	409.5	0	1477.95	51.9	0.30	24.0	4.2	Extended
HOPS-395	05:39:17.09	−07:24:24.64	0.81 × 0.66	−79.9	397.2	0	0.5	31.7	0.09	15.0	2.8	Extended
HOPS-398	05:41:29.42	−02:21:16.44	0.96 × 0.69	−70.0	408.0	0	1.01	23.0	0.11	5.0	/	Extended
HOPS-399	05:41:24.94	−02:18:06.71	0.93 × 0.68	−80.6	407.9	0	6.34	31.1	0.21	67.0	2.0	Extended
HOPS-400	05:42:45.26	−01:16:13.94	0.93 × 0.69	−81.2	415.4	0	2.94	35.0	0.15	50.0	1.5	Extended
HOPS-401	05:46:07.73	−00:12:21.36	0.95 × 0.70	−69.6	426.9	0	0.61	26.0	0.08	16.0	2.3	Extended
HOPS-402	05:46:10.04	−00:12:16.97	0.94 × 0.69	−81.5	426.9	0	0.55	24.2	0.10	4.0	/	Compact
HOPS-403	05:46:27.91	−00:00:52.20	0.94 × 0.69	−81.7	428.2	0	4.14	43.9	0.14	60.0	1.4	Extended
HOPS-404	05:48:07.72	00:33:51.76	0.94 × 0.69	−81.2	430.1	0	0.95	26.1	0.10	6.0	2.3	Compact
HOPS-407	05:46:28.26	00:19:27.90	0.97 × 0.70	−68.3	419.1	0	0.71	26.8	0.08	16.0	2.2	Extended
HOPS-408	05:39:30.90	−07:23:59.80	0.89 × 0.66	−71.0	398.9	0	0.52	37.9	0.06	18.0	2.1	Extended
HOPS-409	05:35:21.37	−05:13:17.93	0.89 × 0.67	−71.0	392.8	0	8.18	28.4	0.13	40.0	2.0	Compact
OMC1N-4-5-ES	05:35:15.97	−05:20:14.28	0.91 × 0.66	−68.8	392.8	/	/	/	0.19	46.0	3.5	Binary
OMC1N-4-5-EN	05:35:16.05	−05:20:05.78	0.91 × 0.66	−68.8	392.8	/	/	/	0.19	46.0	2.6	Binary
OMC1N-4-5-W	05:34:14.26	−05:20:11.65	0.91 × 0.69	−68.9	392.8	Starless	/	/	0.12	/	/	Unresolved
OMC1N-6-7	05:35:15.70	−05:20:39.35	0.91 × 0.66	−69.4	392.8	/	/	/	0.25	98.0	3.6	Extended

Table 1
(Continued)

Name	R.A. (h:m:s)	Decl. (d:m:s)	Beam (arcsec × arcsec)	P.A. (deg)	D (pc)	Class	$L_{\rm bol}$ ($L_\odot$)	$T_{\rm bol}$ (K)	σ_I (mJy)	$\sigma_{^{12}{\rm CO}}$ (mJy)	$\sigma_{{\rm C}^{17}{\rm O}}$ (mJy)	Type Stokes I
OMC1N-8-N	05:35:18.20	−05:20:48.62	0.91 × 0.66	−69.5	392.8	/	/	/	0.19	31.0	3.0	Multiple
OMC1N-8-S	05:35:18.01	−05:20:55.82	0.91 × 0.66	−69.5	392.8	/	/	/	0.19	31.0	3.0	Multiple

Note. Columns (2)−(13) present the R.A., decl., beam size, position angle (P.A.), distance (D), evolutionary stage, bolometric luminosity ($L_{\rm bol}$), bolometric temperature ($T_{\rm bol}$), error of total intensity map (σ_I), error of ^{12}CO image cube ($\sigma_{^{12}{\rm CO}}$), error of C^{17}O image cube ($\sigma_{{\rm C}^{17}{\rm O}}$), and type of Stoke I, respectively. The values D, evolutionary stage, $L_{\rm bol}$, and $T_{\rm bol}$ are obtained from Tobin et al. (2020) and Federman et al. (2023). The Stokes I types are classified by comparing the ratio (R) of the area enclosed by the intensity contour at 0.2 times the maximum to the restoring beam size. Sources with $R < 1$, $1 \leqslant R \leqslant 3$, and $R > 3$ are categorized as "Unresolved," "Compact," and "Extended," respectively; sources are classified as either "Binary" or "Multiple" when there are a two or more well resovled components within 10″ (∼4000 au) from the peak intensity.

Table 2
Spectral Setup

Spectral window	Channels	Rest Frequency (GHz)	Bandwidth (MHz)	Spectral Resolution (MHz)	Velocity Resolution (km s^{-1})
1: CO (3–2)	1920	345.79599	468.75	0.24	0.21
2: continuum	1920	348.50000	1875.00	0.98	0.84
3: continuum	1920	334.50000	1875.00	0.98	0.88
4: continuum*	1920	336.50000	1875.00	0.98	0.87

Note. The fourth spectral window includes C^{17}O, which is marked by an asterisk.

The dust continuum images were produced using the `tclean` task in CASA (CASA Team et al. 2022), with a *Briggs* weighting *robust* parameter set to 0.5, which is a good compromise between resolution and sensitivity (Briggs 1995). The extremely bright line ^{12}CO (3–2) is flagged before self-calibration. Then, we performed three successive rounds of phase-only self-calibration for each source to improve the image quality. The Stokes I image was used as a model for self-calibration, with solution intervals set to 600, 30, and 10 s for the first, second, and third iterations, respectively. To avoid the effects of bright lines on the dust continuum emission, channels exceeding 1.5 times the continuum baseline were flagged after the third round of self-calibration. The final Stokes I, Q, U continuum maps were produced independently using line-free and self-calibrated data of all spectral windows.

The self-calibrated continuum emission (Stokes I) is strongly detected with a signal-to-noise ratio (S/N) ranging from 750 to 4200 for all targets. The average noise level in the final Stokes I image is ∼0.1 mJy beam^{-1}, which is higher than the noise level of $\sigma_{QU} \sim 0.07$ mJy beam^{-1} in both the Stokes Q and U maps. This difference arises from the total intensity image being more dynamic range limited than the polarized intensity images. The debiased polarized intensity is defined as $P = (Q^2 + U^2 - \sigma_{QU}^2)^{1/2}$ (Vaillancourt 2006; Hull & Plambeck 2015), using a $3\sigma_{QU}$ cutoff value. The fractional polarization is derived as $P_{\rm frac} = P/I$. The polarization angle is calculated as $\theta = 0.5 \cdot \arctan(U/Q)$, using a 3σ value of the polarization intensity map as a threshold.

For the line data, we first applied the self-calibration solutions to the entire data set. Then, the full, non-channel-averaged dirty image cubes were produced to identify the channels of continuum. The `uvcontsub` task was used to perform continuum fitting and subtraction in the u-v plane. Finally, we performed the `tclean` task to produce Stokes I, Q, and U image cubes using self-calibrated, continuum-subtracted data for each spectral window.

The ^{12}CO (3–2) and C^{17}O (3–2) channel maps were used to identify the molecular outflows and the molecular emission from the envelope, respectively. The envelope's centroid velocity ($V_{\rm LSR}$) was estimated by fitting a Gaussian to the spectrum obtained from averaging the C^{17}O (3–2) emission within a scale of 1000 au around the position of the protostar. The `immoments` task was used to generate the outflow maps. The blue- and redshifted ^{12}CO (3–2) outflow images were obtained using a velocity range starting from $+/-5$ km s^{-1} with respect to $V_{\rm LSR}$ and included all channels where the emission was at least 5σ. However, in some sources (HOPS-78, HOPS-88, HOPS-124, HOPS-182, HOPS-310, HOPS-340, HOPS-341, HOPS-354, HOPS-361N, HOPS-361S, HOPS-370, HOPS-384, HOPS-399, and OMC1N-6-7) the channels near the $V_{\rm LSR}$ are significantly affected by the spatial filtering of the large-scale emission or by optical depth effects. In these cases we manually selected the channels. The velocity field of the envelope was traced using the C^{17}O (3–2) line, specifically the moment 1 map. This map covers all channels with emission exceeding 3σ. Our sample included nine protostars that had companions in one field (HH270IRS, HOPS-310, HOPS-317S, HOPS-354, HOPS-399, HOPS-400, HOPS-402, HOPS-403, and HOPS-404). Since C^{17}O emission is optically thin in the envelope region (see Appendix C), we select the stronger component and carefully choose which channels to include to minimize any effects from the weaker component.

3. Results

Figure 1 shows the results for typical protostars in the sample. Plots for the entire sample are available in Appendix B. One field, OMC1N-4-5-W, does not show polarization

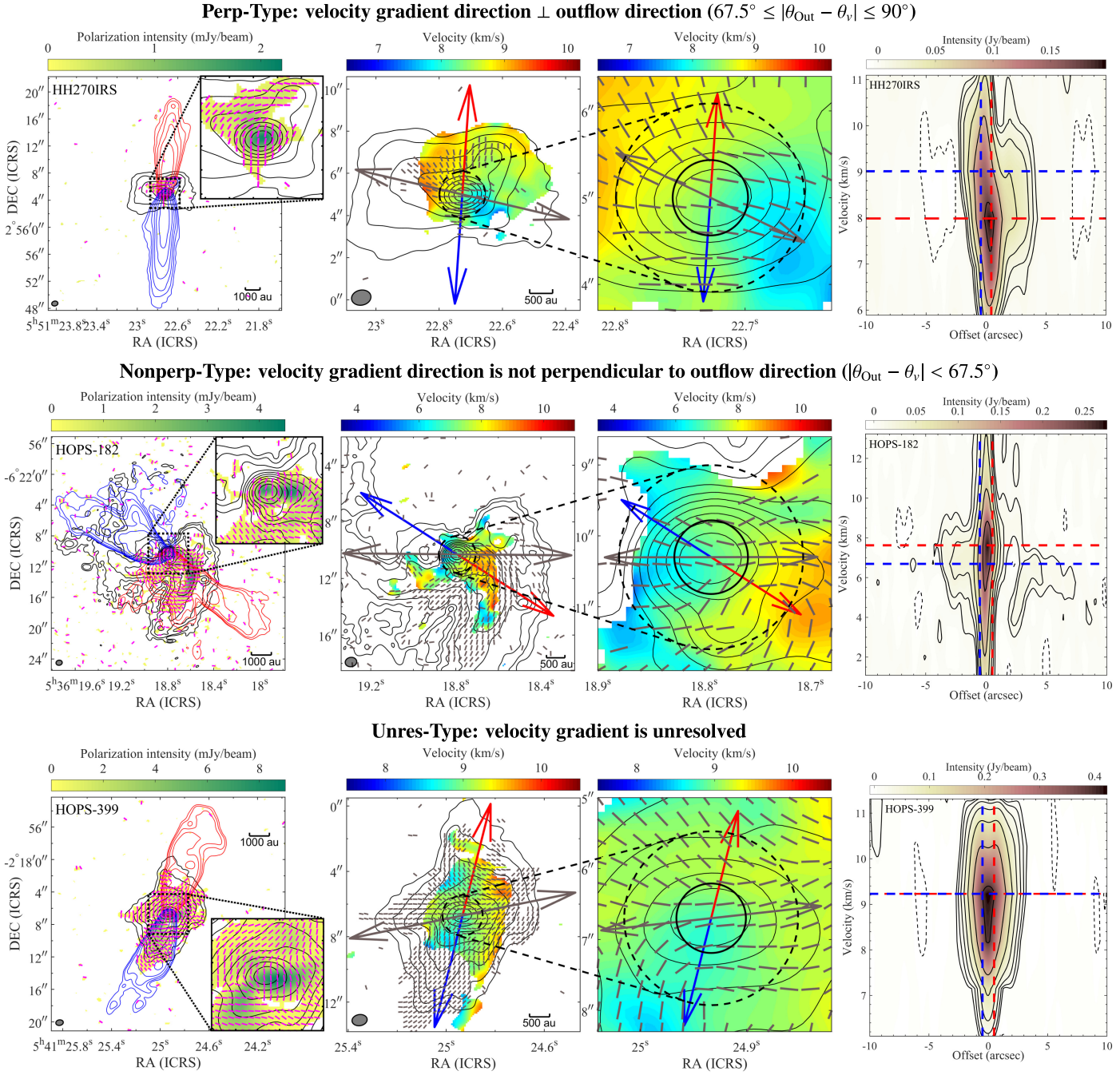

Figure 1. Example maps in the BOPS survey. First column: 870 μm dust polarization intensity in color scale overlaid with the redshifted and blueshifted outflow lobes (obtained from the ^{12}CO (3–2) line), polarization segments, and dust continuum emission (Stokes *I*) contours. Blue contours indicate the blueshifted outflow, while red contours indicate the redshifted outflow, with counter levels set at 5 times the outflow rms × (1, 2, 4, 8, 16, 32). The magenta segments represent the polarization. The regions of polarization intensity less than 3σ have been masked. Second column: the velocity field in color scale (obtained from the C^{17}O (3–2) line) overlaid with the *B*-field segments (i.e., polarization rotated by 90°) and Stokes *I* contours. Third column: an enlarged perspective of 1000 au of the second column. In the second and third panels, the black segments represent the *B*-fields. The red and blue arrows indicate the mean direction of the redshifted and blueshifted outflows, respectively. For the velocity field, regions with an S/N less than 4 have been flagged. The gray arrows in the second and third columns indicate the mean *B*-field directions weighted by the intensity including all the polarization segments and weighted by the uncertainty within an annular region of 400–1000 au, respectively. In the first, second, and third columns, the black contour levels for the Stokes *I* image are 10 times the rms × (1, 2, 4, 8, 16, 32, 64, 128, 256, 512). The black dotted square in the first column corresponds to a scale of 2000 au, while the black dashed and solid circles correspond to scales of 1000 and 400 au, respectively. Fourth column: C^{17}O PV diagram perpendicular to the outflow direction. The color scale indicates the total intensity of the C^{17}O line. Black solid contour levels are 3 times the intensity rms × (1, 2, 4, 8, 16, 32, 64), while dashed contours are set at 3 times the intensity rms × (−1, −2, −4). Vertical dashed lines represent a scale of 400 au, with a blue line indicating a blueshifted offset of 200 au and a red line indicating a redshifted offset of 200 au. The red and blue horizontal lines indicate the velocity values corresponding to the positions with the highest intensity on the 200 au redshifted and blueshifted scales, respectively.

emission or CO (3–2) outflow emission, and the dust peak intensity is weak (∼3 mJy beam^{-1}), signifying that it could be a starless core. In the remaining fields, we successfully detected both dust polarization and molecular outflows in 56 sources, and the dust polarization but no clear outflow in three sources (HOPS-373E, HOPS-398, HOPS-402). Additionally,

we identified two sources (HOPS-87S and OMC1N-8-S) with outflow signature but no polarization detection, which will not be included in this paper. Among these 56 protostars, 47 clearly exhibit the usual red and blue bipolar patterns; the remaining 9 protostars only show one distinct outflow component, with the other being very weak or overlapping with the other outflow lobe.

The properties for the entire sample can be found in Table 1. The position angles of polarization are determined using two different methods: the total-intensity-weighted average, and the uncertainty-weighted average. The position angles of polarization weighted by intensity $\langle\theta_{\rm Pol}\rangle_I$ and uncertainty $\langle\theta_{\rm Pol}\rangle_\sigma$ can be expressed as, respectively,

$$\langle\theta_{\rm Pol}\rangle_I = 0.5 \cdot \arctan\left(\frac{D}{N}\right), \quad \langle\theta_{\rm Pol}\rangle_\sigma = 0.5 \cdot \arctan\left(\frac{K}{M}\right), \tag{1}$$

where N and D are intensity-weighted values of Stokes Q and U, respectively, and M and K are uncertainty-weighted values of Stokes Q and U, respectively (see Appendix A for details). Note that the weighted polarization angle $\langle\theta_{\rm Pol}\rangle$ should be rotated by 90° to infer the mean direction of B-field $\langle\theta_B\rangle$ if the polarization arises from B-field-aligned grains. The outflow direction is estimated by averaging the position angles of the redshifted and blueshifted emission, as discussed in Appendix B. The disk's major axis angles are derived from high-resolution (0.″1, ∼40 au) observations as reported in Tobin et al. (2020). We excluded the disks with a low S/N (<5σ of integrated intensity) and the almost face-on disks (with an inclination angle of <30°). The position angles of polarization ($\langle\theta_{\rm Pol}\rangle$), B-field ($\langle\theta_B\rangle$), outflow ($\theta_{\rm Out}$), and disk ($\theta_{\rm Disk}$) are listed in Tables 3 and 4.

3.1. Self-scattering

Self-scattering polarization is observed parallel to the minor axis of an inclined disk (e.g., Kataoka et al. 2015; Yang et al. 2016a, 2016b; Kataoka et al. 2016; Stephens et al. 2017a; Kataoka et al. 2017); thus, it is expected to be aligned with the outflow direction. Within the BOPS sample with clear outflow detections, there are 17 protostars with compact polarized emission. We performed Gaussian fits to the polarized intensity and found that in each case the upper limits of the size of polarized emission are comparable to disk sizes, suggesting that the polarization arises from disk scales. The deconvolved major and minor axes from the Gaussian fits are consistent with the resolved disk sizes obtained from high-angular-resolution data by Tobin et al. (2020). The top panels of Figure 2 show the distribution of the difference between the polarization direction and the outflow direction (top left panel) and the disk orientation along the major axis (top right panel) in compact polarized sources. In these two plots, for almost all of the sources the polarization angle appears to be perpendicular to the disk major axis and parallel to the outflow. Only HOPS-250 shows a polarization angle perpendicular to the outflow. Excluding this source, we find that the median difference between polarization direction and the outflow direction is 7°, and the median difference between polarization direction and the disk major axis is 86°. The fractional polarization of these 16 protostars is between 0.5% and 2.0%, suggesting that the compact polarization detected arises from self-scattering (e.g., Kataoka et al. 2016; Yang et al. 2017; Girart et al. 2018). The outflow position angle, polarization direction, and disk orientation of these sources are listed in Table 4.

3.2. B-field at Envelope Scales

We are left with 40 protostars associated with a molecular and envelope polarization emission. We do not expect self-scattering to be significant in the envelope because the emission is more isotropic and the grain size is smaller compared to disk scale (Kataoka et al. 2016). Thus, for these cases (including HOPS-250 with compact polarized emission), we assume that the polarization is produced by magnetically aligned grains. Based on this, we classify each protostar based on its B-field pattern, as seen in Figure 3. We find that most of these targets can be classified into three main B-field morphologies: standard hourglass, rotated hourglass, and spiral (note that in many sources there are significant deviations from an ideal spiral shape). In the standard-hourglass category, eight protostars show the expected morphology (e.g., Girart et al. 2006), in which their outflow is roughly parallel to the direction of the hourglass axis. There are 13 protostars that exhibit a similar hourglass structure, but flipped by 90°, such that its axis is perpendicular to the outflow; these are classified as rotated hourglass. The spiral category encompasses nine protostars with well-organized or partial spiral patterns in their B-field structure (as in, e.g., Sanhueza et al. 2021). In addition to these three categories, five protostars exhibit a B-field pattern that is complex, and five do not have enough data (see Table 3). In the case of a rotated-hourglass B-field morphology, all protostars with this shape in our sample exhibit extended polarized emission; thus, the potential ambiguity with self-scattering is not important. Moveover, there are six protostars in our sample that have polarized emission that appears to be along streamer-like dust structures (HOPS-168, HOPS-182, HOPS-361N, HOPS-361S, HOPS-370, and OMC1N-8-N, as shown in Appendix B). The B-field in each of these protostars appears to follow the direction of this streamer-like structure.

As shown by the peripheral vectors in all panels of Figure 1 (particularly in the HOPS-182 field), 3σ polarized emission in some regions may be generated by noise in the data; we therefore performed a total-intensity-weighted average B-field using a $4\sigma_{QU}$ threshold in our polarization emission data (see Appendix A). The bottom left panel of Figure 2 shows the histogram of the angle difference between the outflow and these average B-field directions. The distribution appears almost random. However, there is a slight preference for the cases where the outflow is perpendicular to the B-field direction: two-fifths of the protostars (16 out of 40) are located in the last quartile (angle difference in the 67°.5–90° range).

3.3. B-field at Scales of 400–1000 au

The use of the intensity-weighted average B-field direction, as used by Hull et al. (2014), favors the polarization signal around the dust peak intensity, which may have significant contributions from both total and polarized emission in the circumstellar disk. In the BOPS sample, the disks have radii

Table 3
Parameters of the Entire Sample

Name	$\theta_{\rm Out}$ (deg)	$\Delta\theta_{\rm Out}$ (deg)	$\langle\theta_{B_1}\rangle_I$ (deg)	$\langle\theta_{B_2}\rangle_I$ (deg)	$\langle\theta_B\rangle_\sigma$ (deg)	θ_v (deg)	$\lvert\nabla v_{\rm abs}\rvert$ (km s^{-1} arcsec^{-1})	$\theta_{\rm Disk}$ (deg)	$\theta_{\rm Inc}$ (deg)	Type *B*-field
Perp-Type										
HH270IRS	176.1 ± 6.6	92.7	76.9	68.9 ± 0.8	64.4 ± 7.0	64.6 ± 1.8	1.2	87.4	58.8	Rot-hourglass
HOPS-78	81.0 ± 5.6	69.6	176.3	172.3 ± 0.5	175.0 ± 3.5	153.4 ± 6.6	1.3	171.1	71.4	Rot-hourglass
HOPS-88	81.1 ± 5.6	90.4	31.5	32.8 ± 1.4	27.9 ± 5.1	149.3 ± 4.0	1.3	166.9	25.8	Complex
HOPS-96	49.1 ± 5.6	75.1	113.3	100.0 ± 1.6	101.5 ± 2.6	123.2 ± 6.8	1.1	134.6	23.6	Spiral
HOPS-124	75.4 ± 5.7	66.6	127.1	153.7 ± 3.0	155.9 ± 9.5	164.0 ± 3.6	2.8	3.3	44.4	Spiral
HOPS-288	39.4 ± 5.8	47.6	124.2	122.8 ± 0.4	119.4 ± 3.5	118.3 ± 3.8	3.7	145.6	64.6	Rot-hourglass
HOPS-409	19.0 ± 5.6	51.8	113.9	102.3 ± 1.0	92.3 ± 2.3	115.7 ± 2.9	2.0	115.8	69.3	Rot-hourglass
OMC1N-4-5-ES	53.9 ± 5.6	72.2	155.9	164.3 ± 0.7	160.6 ± 2.3	153.4 ± 13.8	1.1	/	/	Rot-hourglass
Nonperp-Type										
HOPS-182	57.4 ± 5.5	82.3	89.5	99.1 ± 0.4	90.1 ± 3.0	74.9 ± 2.2	1.2	150.8	60.7	Spiral
HOPS-310	136.5 ± 5.9	75.0	48.9	49.3 ± 0.7	46.6 ± 2.6	116.7 ± 3.9	2.2	45.7	58.9	Rot-hourglass
HOPS-341	63.6 ± 6.2	65.4	8.2	14.3 ± 8.3	17.1 ± 22.2	177.1 ± 2.0	1.2	145.8	53.1	Not enough data
HOPS-361N	26.1 ± 6.2	59.7	42.0	53.6 ± 0.7	71.2 ± 6.4	166.4 ± 2.0	3.3	130.1	66.2	Spiral
HOPS-361S	26.6 ± 8.7	79.8	170.4	178.3 ± 2.3	166.4 ± 6.7	147.7 ± 5.0	1.2	14.4	54.8	Spiral
HOPS-404	134.9 ± 17.4	89.8	70.9	90.9 ± 0.9	102.9 ± 6.2	99.0 ± 4.2	1.1	144.2	0	Spiral
Unres-Type										
HOPS-11	137.9 ± 5.6	42.7	145.6	150.6 ± 2.0	151.9 ± 7.9		$\lesssim$1.0	94.4	22.6	Std-hourglass
HOPS-12W	127.9 ± 7.9	124.5	46.6	21.3 ± 1.4	23.2 ± 6.4		$\lesssim$1.0	103.3	33.6	Complex
HOPS-87N	173.4 ± 7.0	62.7	37.5	36.1 ± 0.1	42.5 ± 2.0		$\lesssim$1.0	11.1	13.5	Std-hourglass
HOPS-164	64.2 ± 5.5	56.4	170.2	168.3 ± 4.3	166.0 ± 5.0		$\lesssim$1.0	150.8	50.5	Not enough data
HOPS-168	168.4 ± 5.5	89.4	65.0	64.0 ± 0.9	51.8 ± 3.6		$\lesssim$1.0	127.1	46.2	Rot-hourglass
HOPS-169	174.2 ± 5.5	43.1	66.9	48.4 ± 1.2	45.5 ± 4.6		$\lesssim$1.0	61.5	40.1	Rot-hourglass
HOPS-224	79.7 ± 6.3	62.0	65.9	71.4 ± 1.7	73.3 ± 5.4		$\lesssim$1.0	170.4	51.6	Std-hourglass
HOPS-303	66.5 ± 5.9	68.5	95.6	118.6 ± 2.4	120.4 ± 10.7		$\lesssim$1.0	164.0	37.7	Spiral
HOPS-317N	39.4 ± 6.3	94.3	75.4	79.7 ± 3.5	80.2 ± 1.3		$\lesssim$1.0	48.3	25.8	Not enough data
HOPS-317S	87.2 ± 17.3	78.7	7.3	10.1 ± 0.3	3.8 ± 5.2		$\lesssim$1.0	92.2	45.4	Rot-hourglass
HOPS-325	17.1 ± 6.1	56.4	157.3	154.9 ± 2.1	146.1 ± 5.9		$\lesssim$1.0	119.0	25.8	Rot-hourglass
HOPS-359	71.6 ± 2.5	23.6	50.6	49.7 ± 0.3	56.0 ± 6.7		$\lesssim$1.0	3.6	28.1	Std-hourglass
HOPS-370	16.7 ± 5.6	114.5	110.5	108.4 ± 0.3	109.9 ± 2.0		$\lesssim$1.0	109.7	71.1	Rot-hourglass
HOPS-373W	89.2 ± 6.1	72.4	35.0	30.9 ± 1.0	25.1 ± 4.6		$\lesssim$1.0	144.3	25.8	Std-hourglass
HOPS-384	104.5 ± 9.2	50.0	6.4	172.1 ± 0.2	172.4 ± 2.6		$\lesssim$1.0	60.2	45.6	Spiral
HOPS-395	1.4 ± 8.0	54.4	44.3	2.6 ± 1.0	1.5 ± 4.1		$\lesssim$1.0	79.9	0	Complex
HOPS-399	163.9 ± 5.8	78.0	101.5	96.4 ± 0.1	96.3 ± 3.6		$\lesssim$1.0	143.6	37.9	Complex
HOPS-400	81.1 ± 6.0	83.8	90.1	93.3 ± 0.2	95.4 ± 2.7		$\lesssim$1.0	18.5	21.3	Std-hourglass
HOPS-401	69.7 ± 4.3	30.8	144.4	148.4 ± 1.7	148.5 ± 6.3		$\lesssim$1.0	176.9	40.4	Rot-hourglass
HOPS-403	62.2 ± 6.1	70.5	134.3	107.9 ± 1.6	104.5 ± 8.8		$\lesssim$1.0	64.0	13.0	Spiral
HOPS-407	98.9 ± 7.5	39.0	88.8	88.2 ± 0.3	82.4 ± 2.3		$\lesssim$1.0	173.6	38.9	Std-hourglass
HOPS-408	85.7 ± 8.2	83.5	17.3	10.5 ± 1.0	10.2 ± 1.5		$\lesssim$1.0	157.5	31.0	Not enough data
OMC1N-4-5-EN	113.7 ± 5.6	35.9	76.4	74.5 ± 0.6	71.2 ± 2.8		$\lesssim$1.0	/	/	Complex
OMC1N-6-7	72.7 ± 5.6	103.4	18.7	12.8 ± 1.5	17.2 ± 5.8		$\lesssim$1.0	/	/	Rot-hourglass
OMC1N-8-N	130.9 ± 5.6	61.2	117.8	122.3 ± 0.7	125.8 ± 2.5		$\lesssim$1.0	/	/	Std-hourglass
Other										
HOPS-250	134.5 ± 6.1	98.6	142.2	/	/		$\lesssim$1.0	43.4	53.6	Not enough data
HOPS-373E	/	/	145.0	149.1 ± 1.0	154.9 ± 4.6	/	/	144.3	25.8	Complex
HOPS-398	/	/	92.5	52.4 ± 1.6	20.0 ± 9.0	/	/	10.6	30.3	Complex
HOPS-402	/	/	90.3	90.9 ± 0.7	90.6 ± 1.0	/	/	58.7	47.6	Not enough data
HOPS-87S	58.7 ± 8.0	86.5	/	/	/	/	/	/	/	/
OMC1N-8-S	120.2 ± 7.0	99.3	/	/	/	/	/	/	/	/
OMC1N-4-5-W	/	/	/	/	/	/	/	/	/	/

Note. Columns (2)–(11) present the outflow position angle ($\theta_{\rm Out}$), outflow mean open angle ($\Delta\theta_{\rm Out}$), intensity-weighted *B*-field position angle within the field of view ($\langle\theta_{B_1}\rangle_I$) and within 400–1000 au ($\langle\theta_{B_2}\rangle_I$), uncertainty-weighted *B*-field position angle within 400–1000 au ($\langle\theta_B\rangle_\sigma$), position angle of velocity gradient (θ_v), absolute velocity gradient ($\lvert\nabla v_{\rm abs}\rvert$), disk orientation along the major axis ($\theta_{\rm Disk}$), the inclination angle of the disk ($\theta_{\rm Inc}$), and the type of *B*-field morphology, respectively. $\theta_{\rm Disk}$ and $\theta_{\rm Inc}$ are obtained from Tobin et al. (2020). The type of *B*-field is classified as Standard Hourglass (Std-hourglass), Rotated Hourglass (Rot-hourglass), Spiral, Complex, and Not enough data.

Table 4
Self-scattering Sources

Name	$\theta_{\rm Out}$ (deg)	$\Delta\theta_{\rm Out}$ (deg)	$\langle\theta_{\rm Pol}\rangle_I$ (deg)	$\theta_{\rm Disk}$ (deg)	$\theta_{\rm Inc}$ (deg)
HH212M	23.5 ± 6.1	51.2	27.9 ± 0.4	118.6	63.0
HOPS-10	37.6 ± 5.6	75.2	30.6 ± 2.3	116.6	60.0
HOPS-12E	152.5 ± 5.6	41.7	147.7 ± 2.9	76.6	38.9
HOPS-50	164.1 ± 7.9	115.5	147.3 ± 0.8	68.3	58.7
HOPS-53	14.4 ± 5.6	69.9	37.5 ± 2.1	128.7	44.4
HOPS-60	61.1 ± 5.6	86.3	74.7 ± 0.6	159.0	54.6
HOPS-81	30.0 ± 5.6	72.8	52.7 ± 3.1	122.0	53.1
HOPS-84	83.7 ± 5.6	62.4	78.1 ± 0.4	167.5	62.5
HOPS-153	127.0 ± 5.6	44.6	120.8 ± 0.6	32.4	75.1
HOPS-203N	139.2 ± 5.5	50.6	141.1 ± 0.6	50.2	67.1
HOPS-203S	97.3 ± 7.8	50.2	92.9 ± 1.5	175.4	53.1
HOPS-247	110.0 ± 7.7	91.9	105.3 ± 0.5	17.9	45.9
HOPS-340	7.2 ± 6.2	55.6	24.9 ± 3.6	99.7	50.5
HOPS-354	52.4 ± 5.1	100.3	57.2 ± 3.2	158.6	29.0
HOPS-358	156.2 ± 6.1	57.5	171.5 ± 0.7	81.2	74.7
HOPS-383	139.2 ± 5.6	52.0	130.3 ± 1.2	49.7	48.2

Note. Columns (2)–(6) present the outflow position angle ($\theta_{\rm Out}$), outflow mean open angle ($\Delta\theta_{\rm Out}$), intensity-weighted position angle of polarization within the inner 400 au scale ($\langle\theta_{\rm Pol}\rangle_I$), disk orientation along the major axis ($\theta_{\rm Disk}$), and the inclination angle of the disk ($\theta_{\rm Inc}$), respectively. $\theta_{\rm Disk}$ and $\theta_{\rm Inc}$ are obtained from Tobin et al. (2020).

between 30 and 250 au (0.″08 and 0.″63; Tobin et al. 2020). To avoid possible contamination from disk self-scattering polarization (see Section 3.1), we select an annular region from 1″ (∼400 au) to 2.″5 (∼1000 au). Within this region the difference between the outflow and the intensity-weighted average *B*-field direction appears to be very similar to the one obtained using all polarization data (as shown in the bottom panels of Figure 2).

The envelope kinematics are traced by optically thin $C^{17}O$ emission (see Appendix C). The envelope's angular momentum is expected to be parallel to the outflow (Pudritz & Ray 2019). We generated position–velocity (PV) cuts from the $C^{17}O$ (3–2) channel maps centered at the dust peak intensity and perpendicular to the outflow axis. We calculated the absolute velocity gradient ($|\nabla v_{\rm abs}|$) in the PV image by selecting the most redshifted/blueshifted emission at 5σ at a distance of 400 au from the protostar position (as shown in Column (8) of Table 3). We found significant velocity gradients (i.e., $|\nabla v_{\rm abs}| \gtrsim 1.0\,{\rm km\,s^{-1}\,arcsec^{-1}}$) toward 14 protostars, which is probably indicative of rotation. However, most of the sources do not show a clear gradient, which may due to the limited spectral resolution of the observations (∼0.9 $\rm km\,s^{-1}$). In addition, we use the moment 1 (intensity-weighted velocity) maps of the $C^{17}O$ (3–2) emission to derive the direction of the velocity gradient. To do so, we fit a 2D linear regression fit to the moment 1 map following Goodman et al. (1993) and Tobin et al. (2011). Further details regarding envelope kinematics are discussed in Appendix C. Column (7) in Table 3 lists the velocity gradient position angle. In cases without a significant velocity gradient, we use the spectral resolution divided by the angular resolution as an upper limit. We use the velocity gradient position angle θ_v and outflow direction $\theta_{\rm Out}$ (as depicted in Figure 1) to classify the protostars into three types. This is done for 39 protostars where significant polarization data are detected within the annular region of 400–1000 au:

1. Perp-Type: velocity gradient is perpendicular to the outflow ($67.^\circ5 \leqslant |\theta_{\rm Out} - \theta_v| \leqslant 90^\circ$; 8 out of 39).
2. Nonperp-Type: velocity gradient is not perpendicular to the outflow ($|\theta_{\rm Out} - \theta_v| < 67.^\circ5$; 6 out of 39).
3. Unres-Type: velocity gradient is unresolved ($|\nabla v_{\rm abs}| \lesssim 1.0\,{\rm km\,s^{-1}\,arcsec^{-1}}$; 25 out of 39).

We use the uncertainty-weighted position angles of the *B*-field on scales of 400–1000 au (represented as $\langle\theta_B\rangle_\sigma$) for the following analysis, which are listed in Column (6) of Table 3. The left panel of Figure 4 shows the distribution of the *B*-field and outflow direction for the three source types. We find no significant relation between the average *B*-field and the outflow directions in Nonperp-Type and Unres-Type. However, in Perp-Type sources, a correlation between the *B*-field and outflow is evident, with a correlation coefficient of 0.83 between $|\langle\theta_B\rangle_\sigma - 90^\circ|$ and outflow position angle $\theta_{\rm Out}$. Specifically, 75.0% (±12.5%) of the sources show a trend that the *B*-field is perpendicular to the outflow.

We obtained the disk orientation of 20 sources from Tobin et al. (2020), 5 in Perp-Type, 5 in Nonperp-Type, and 10 in Unres-Type. As shown in the right panel of Figure 4, due to the small sample size in each group, it is difficult to characterize the correlation between the *B*-field and the disk orientation. Globally, there seems to be random alignment between the *B*-field and the disk orientation within the 20 sources. However, we find some trends for the Perp-Type sources, with almost all showing parallel alignment between the mean *B*-field and disk orientation, with a correlation coefficient of 0.96.

3.4. Geometric Projection Effect

The position angles of the outflow and *B*-field we measured are projected onto the plane of the sky. To investigate the influence of projection effects on our results, we plot the cumulative distribution function (CDF) of the observed angle difference (Hull et al. 2013, 2014; Stephens et al. 2017a) and compare it with 2D simulated intersecting angles uniformly projected from a 3D space. The parallel case uses the angles randomly selected within 0 and 22.°5 in 3D and then projected onto the plane of the sky in the simulation, while the ranges of 3D angles used in random and perpendicular cases are 0°–90° and 67.°5–90°, respectively. For simplicity, it is prudent to exclusively employ the 3D projection analysis on the entire sample only (i.e., not in any of the other subsamples analyzed in this work), represented in Figure 5.

We run the Kolmogorov–Smirnov (K-S) test on the angle difference distribution of our sample. When considering the difference between the *B*-fields and outflow directions in all 39 sources, we compared the observed distribution with the simulated models. The probability of our results being drawn from parallel models is <0.001, ruling out this scenario. The probability that the distribution is drawn from a random model is 0.325, and the probability that it is drawn from a perpendicular model is 0.615. Though the probability is higher for the perpendicular case, each model could be possible for the distribution.

4. Discussion

The polarization properties in approximately one-third of the sample (16) strongly suggest that they are tracing self-scattering in disks. Most of these targets are Class 0 (except for the Class I source of HOPS-84), and their bolometric

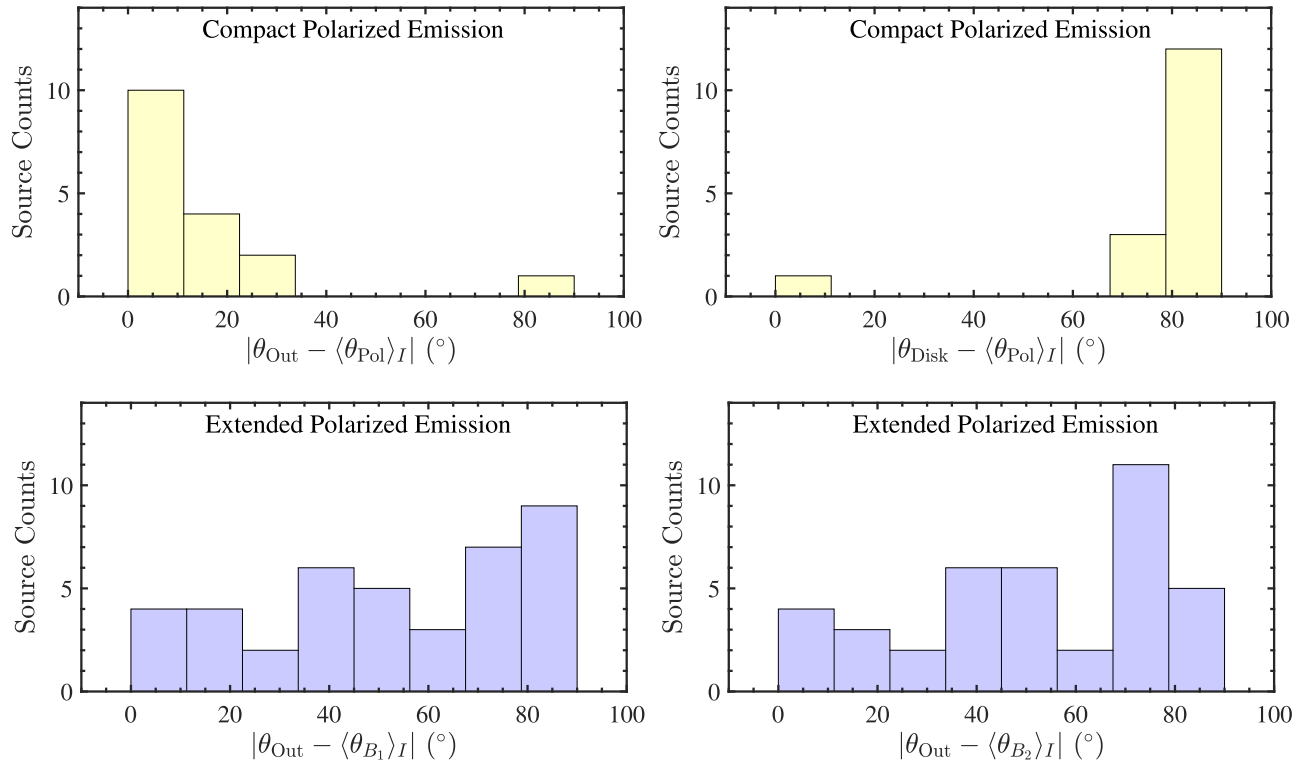

Figure 2. Histograms of angle's differences for the 17 protostars with compact, barely resolved polarized emission thought to be related to dust polarization caused by dust self-scattering (top panels) and for the rest of the protostars with extended polarized emission (bottom panels). Top panels: histogram of the angle difference between the outflow direction $\theta_{\rm Out}$ and the mean polarization direction weighted by the intensity $\langle\theta_{\rm Pol}\rangle_I$ (left) and between the disk orientation along the major axis $\theta_{\rm Disk}$ and the mean polarization direction $\langle\theta_{\rm Pol}\rangle_I$ (right). In the histogram in the top right panel, one disk, from HOPS-354, is not included because the disk is probably nearly face-on. Bottom panels: histogram of the angle difference between the outflow direction $\theta_{\rm Out}$ and the intensity-weighted average *B*-field direction using all the detected polarized emission $\langle\theta_{B_1}\rangle_I$ (left) and within an annular region with inner and outer radii of 400 and 1000 au $\langle\theta_{B_2}\rangle_I$ (right), respectively. HOPS-250 is not included in the bottom right panel because there is no 4σ polarization detection within the annular region.

temperature is similar to protostars without self-scattering (see Table 1), indicating that self-scattering is independent of evolutionary stages. This result suggests that grain growth has already occurred in the disks in the earliest stages of the protostellar phase. It is possible that other sources in the sample also have polarized emission from self-scattering, but this would only be apparent around the intensity peak. Higher angular resolution observations are needed to properly quantify disk self-scattering in the full sample (see Liu et al. 2023).

Past interferometric polarization surveys using CARMA probed 16 protostars (Hull et al. 2013) and 30 star-forming cores (Hull et al. 2014) and showed that the *B*-fields are randomly oriented with outflows on a scale of a few thousand au. Subsequently, Zhang et al. (2014) presented SMA observations of 14 massive clumps. They also found that the *B*-fields, on a core scale of 0.01–0.1 pc, do not correlate with the outflow direction. Arce-Tord et al. (2020) found the same results using 1 mm ALMA observations toward 29 protostellar dense cores in high-mass star-forming regions at a scale of 2700 au. In our study, both the histogram of the difference between the outflow and the averaged *B*-field direction (bottom panels of Figure 2) and the CDF of these angle differences (Figure 5) show that the *B*-field is almost perpendicular to the outflow axis in a significant number of protostars. However, there is also a large fraction of protostars where the distribution of the angle difference appears random. These results of relative orientation probably depend on the sample of observed *B*-field morphologies. Other causes may also explain the differences with previous results in the comparison between the mean *B*-field and the outflow axis. The objects in Zhang et al. (2014) are at much greater distances, so they trace much larger linear scales of the *B*-fields. Hull et al. (2013) had a smaller sample of protostars that spanned multiple cores and lacked sensitivity, thus mapping fewer *B*-field vectors. Nevertheless, our results are in agreement with the recent numerical study done by Machida et al. (2020). They found that angular momentum, outflow, and local *B*-field axes depend on the initial angle difference between the angular momentum and the *B*-field axes, as well as at which scales these directions are measured. Galametz et al. (2020) found, in a sample of 20 Class 0 protostars, that the misalignment angle of the *B*-field orientation with the outflow is strongly correlated with the amount of angular momentum on a 1000 au scale. We find similar results for 7 out of 14 sources with strong velocity gradients (the Perp-Type and the Nonperp-Type): their *B*-field direction is perpendicular to the outflow axis.

Several BOPS protostars shows the expected hourglass *B*-field along the outflow axis. This morphology is predicted in the classical models of star formation where the core is initially threaded with a uniform *B*-field, and turbulence and angular momentum are not dynamically important (e.g., Galli et al. 2006). All the protostars with the standard-hourglass shape in our sample are observed in the Unres-Type, possibly because the *B*-field is strong enough to slow down the rotation in this case, or because the core's initial angular velocity was

B-field morphology		Number	Velocity gradient VS outflow direction		
			Perp-Type (8)	Nonperp-Type (6)	Unres-Type (25)
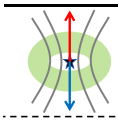	Standard-hourglass	8	0	0	8
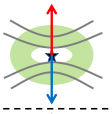	Rotated-hourglass	13	5	1	7
	Spiral	9	2	4	3
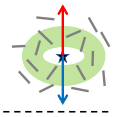	Complex	5	1	0	4
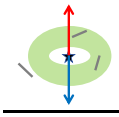	Not enough data	5*	0	1	3
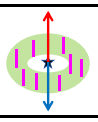	Self-scattering	16	9	3	4

Figure 3. Number of protostars for different types of *B*-field morphology. In the first column, green rings indicate protoplanetary envelope (disk for self-scattering), and star symbols located at the center indicate protostars. Red and blue arrows indicate the outflow directions. Black curves and segments indicate the *B*-field orientation, while magenta segments indicate polarization direction. HOPS-250, which does not have 4σ polarization detection within the annular region from 400 to 1000 au scale, is included in the type of Not enough data, which is marked by the asterisk.

energetically less important than the *B*-field. Most of the protostars with strong envelope velocity gradients (Perp-Type and Nonperp-Type) appear to have a rotated-hourglass or a spiral *B*-field morphology. The rotated-hourglass shape tends to have field lines parallel to the velocity gradients and perpendicular to the outflows; however, in most cases of the spiral shape, the envelope *B*-field does not align with either the velocity gradient or the outflow. In the case of the spiral morphology, this shape could be due to an initial misalignment between *B*-fields and rotation. MHD simulations show that this shape generates magnetic torques, which creates two inflowing spirals aligned with the *B*-field (Wang et al. 2022). This is what is observed in HOPS-182, HOPS-361S, and possibly HOPS-361N (and previously in IRAS18089–1732; Sanhueza et al. 2021). The rotated hourglass could be the extreme case of the standard hourglass, where gravity is so strong (i.e., with a relatively high initial mass-to-flux ratio; see Maury et al. 2018) that the bending of the lines appears perpendicular to the outflow axis, but this may happen only in the innermost part of the envelope as seen in B335 (Maury et al. 2018) and L1448 IRS 2 (Kwon et al. 2019). Alternatively, this could trace the transition from the standard poloidal hourglass to a toroidal *B*-field, due to the effect of an initially large angular momentum (e.g., Machida et al. 2007).

Finally, there are few protostars that clearly show filament- or streamer-like dust structures with the *B*-field along the filament (HOPS-168, HOPS-182, HOPS-361N, HOPS-361S, HOPS-370, and OMC1N-8-N, as shown in Appendix B). We speculate that these could be accretion streamers (e.g., Alves et al. 2020; Pineda et al. 2020; Fernández-López et al. 2023); however, higher spectral resolution observations are needed to confirm this.

5. Summary

We have presented the first results of the BOPS survey, which targets 61 protostars in the OMC star-forming complex. The outflow structure was traced using ^{12}CO (3–2), while the velocity field in the dense region was mapped using C^{17}O (3–2). We detect 870 μm dust polarization emission and outflows around 56 protostars. The main results are as follows:

1. Self-scattering is observed in 16 sources, most of which are Class 0, indicating that grain growth in disks occurs in the very early stages of the disk evolution.
2. Dust polarization traces the *B*-field in 40 protostars at envelope scales (up to ~3000 au). Most of these targets can be classified into three major *B*-field morphologies: the standard hourglass, rotated hourglass (which may be a highly pinched, standard hourglass), and a spiral configuration. These morphologies are the result of the complex interplay between gravitational collapse, *B*-fields, and rotational motions during the star formation process. The *B*-fields aligned with the filament- or streamer-like structure could be related to accretion streamers, but high spectral resolution observations are needed to confirm this scenario.

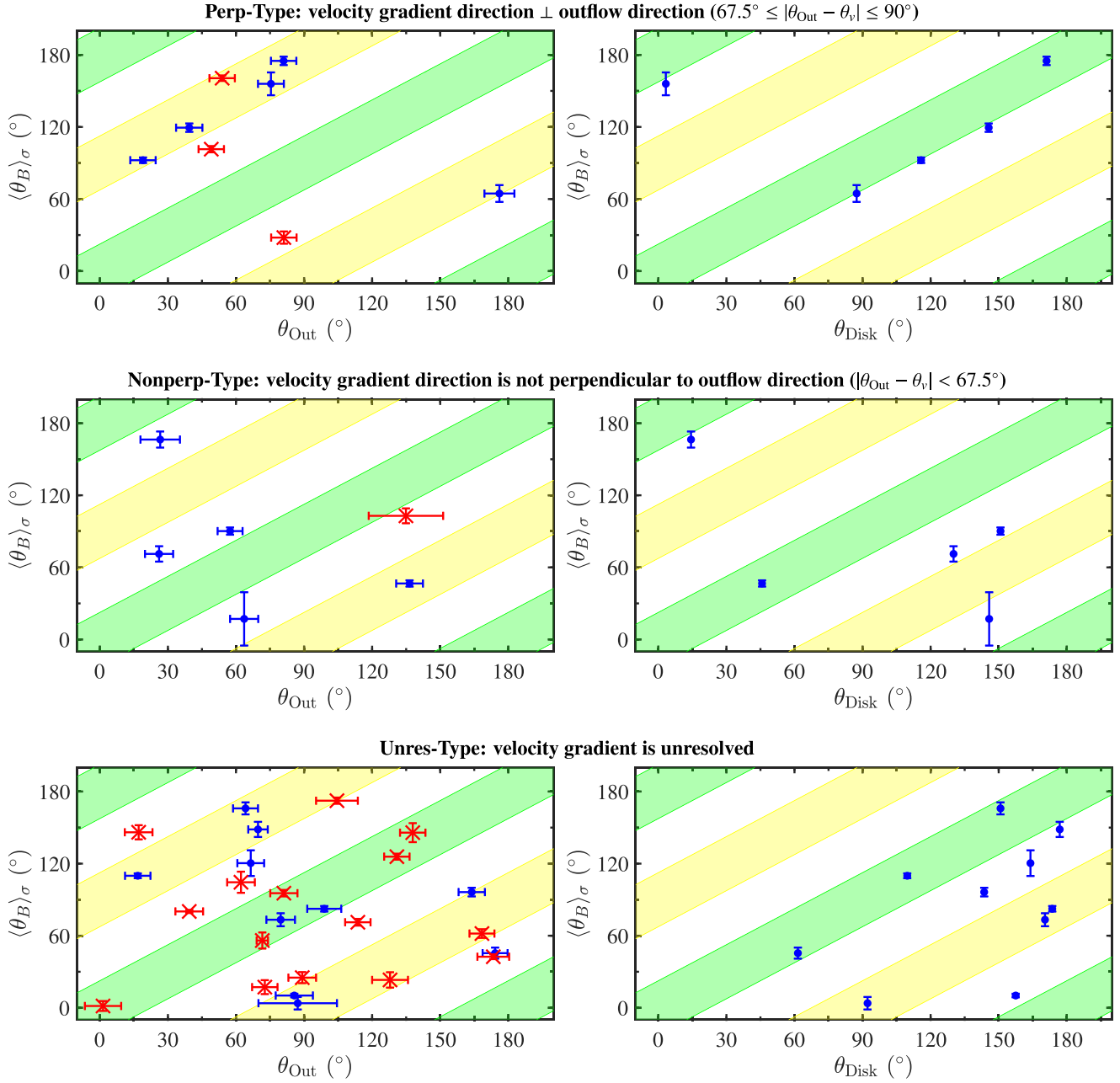

Figure 4. Distribution between the uncertainty-weighted mean *B*-field direction $\langle\theta_B\rangle_\sigma$ and outflow direction $\theta_{\rm Out}$ (left panel) and between the mean *B*-field $\langle\theta_B\rangle_\sigma$ and disk orientation $\theta_{\rm Disk}$ (right panel). In both panels, yellow stripes indicate cases where the two vectors are perpendicular to each other ($67.^\circ5 \leqslant |\theta_{\rm Diff}| \leqslant 90^\circ$), while green stripes represent cases where the two vectors are aligned ($|\theta_{\rm Diff}| \leqslant 22.^\circ5$). Blue circles and red crosses indicate protostars with and without clear disk orientation, respectively.

3. Two-fifths of our sample exhibit an averaged *B*-field that is perpendicular to the outflow; however, the remaining three-fifths of our sample have a random relative orientation. On scales of 400–1000 au, the sources with a strong velocity gradient perpendicular to the outflow axis (Perp-Type) have a *B*-field that is also perpendicular to the outflow axis.
4. Most of the protostars with strong velocity gradients $|\nabla v_{\rm abs}| \geqslant 1.0$ km s^{-1} arcsec^{-1} (Perp-Type and Nonperp-Type) tend to have a rotated-hourglass or spiral *B*-field morphology. In rotated-hourglass *B*-field morphologies, the *B*-field strength is probably less significant with regard to gravity and angular momentum, whereas in spiral structures, the rotation motions seem to be strong enough to twist the field lines, contributing to a helical *B*-field morphology. Notably, all of the sources with *B*-field patterns showing a standard-hourglass structure of *B*-field are in the Unres-Type, i.e., sources without strong velocity gradients, probably due to the magnetic braking.

In summary, three main *B*-field configurations are observed in our study; the rotated-hourglass field shape is more prevalent when the *B*-field strength is less significant compared to gravity and angular momentum, while strong rotation tends to give rise to spiral field structures. In contrast, standard-hourglass field patterns are more commonly observed in sources lacking strong velocity gradients.

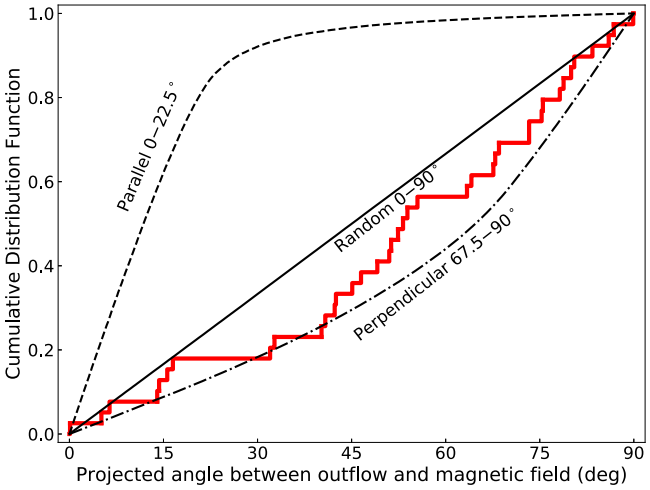

Figure 5. CDF of the projected angles. The red polyline is the observed angle difference between the outflow direction $\theta_{\rm Out}$ and uncertainty-weighted mean B-field direction $\langle\theta_B\rangle_\sigma$. The black solid line, dashed line, and dotted–dashed line indicate Monte Carlo simulations of the expected projected angle for two vectors that are 3D random (difference angle of two vectors is between 0°and 90°), parallel (0°–22.°5), and perpendicular (67.°5–90°), respectively.

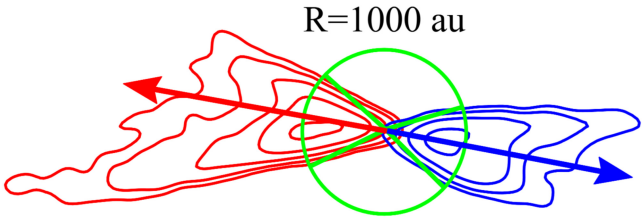

Figure 6. Diagram to identify the position angle of outflows.

Acknowledgments

We thank Jacob Labonte for early analysis of the BOPS data. B.H., J.M.G., and A.S.-M. acknowledge support by grant PID2020-117710GB-I00 (MCI-AEI-FEDER, UE). B.H. also acknowledges financial support from the China Scholarship Council (CSC) under grant No. 202006660008. This work is also partially supported by the program Unidad de Excelencia María de Maeztu CEX2020-001058-M. A.S.-M. acknowledges support from the RyC2021-032892-I grant funded by MCIN/AEI/10.13039/501100011033 and by the European Union "Next GenerationEU"/PRTR. E.G.C. acknowledges support from the National Science Foundation through the NSF MPS Ascend Fellowship grant No. 2213275. L.W.L. acknowledges support by NSF AST-1910364 and NSF AST-2307844. P.S. was partially supported by a Grant-in-Aid for Scientific Research (KAKENHI Nos. JP22H01271 and JP23H01221) of JSPS. W.K. was supported by the National Research Foundation of Korea (NRF) grant funded by the Korean government (MSIT) (NRF-2021R1F1A1061794). Z.Y.L. acknowledges support in part by NASA 80NSSC20K0533 and NSF AST-2307199. This paper makes use of the following ALMA data: ADS/JAO.ALMA#2019.1.00086. ALMA is a partnership of ESO (representing its member states), NSF (USA) and NINS (Japan), together with NRC (Canada), MOST and ASIAA (Taiwan), and KASI (Republic of Korea), in cooperation with the Republic of Chile. The Joint ALMA Observatory is operated by ESO, AUI/NRAO and NAOJ.

Appendix A
Weighted Mean B-field Position Angle

To trace the mean orientation of polarization for these protostars, we extract the size ranging from several hundred to several thousand au, encompassing all polarization measurements toward the targeted source, i.e., all Stokes Q and U pixels larger than 4σ are enclosed. We then calculate its position angle $\langle\theta\rangle$ by performing a total-intensity-weighted average, giving more weight to polarization directions in higher-density regions (Hull et al. 2013, 2014). To guarantee adequate sampling of the derivatives in each pixel, the pixel size used here falls within a region of one-third to half of the beam FWHM (e.g., Soler et al. 2017). For example, in the case of HH212M, with major and minor axes of 0.″95 and 0.″70, respectively, and a beam FWHM of ∼0.″83, the pixel size should be within the range of 0.″28–0.″42. The calculation of intensity-weighted position angle of polarization $\langle\theta_{\rm Pol}\rangle_I$ is expressed as

$$\langle\theta_{\rm Pol}\rangle_I = 0.5\cdot\arctan\left(\frac{D}{N}\right). \tag{A1}$$

N and D are averaged values of Stokes Q and U weighted by the intensity:

$$N=\frac{\sum\limits_{ij}(Q(i,j)\cdot I(i,j))}{\sum\limits_{ij}I(i,j)},\quad D=\frac{\sum\limits_{ij}(U(i,j)\cdot I(i,j))}{\sum\limits_{ij}I(i,j)}, \tag{A2}$$

where i and j are pixel numbers and $I(i,j)$, $Q(i,j)$, and $U(i,j)$ indicate the corresponding values in the (i,j) pixel of the Stokes I, Q, and U images, respectively. The error is estimated through error propagation:

$$\Delta\langle\theta_{\rm Pol}\rangle_I=\sqrt{\left(\frac{\partial\langle\theta_{\rm Pol}\rangle_I}{\partial N}\cdot\Delta N\right)^2+\left(\frac{\partial\langle\theta_{\rm Pol}\rangle_I}{\partial D}\cdot\Delta D\right)^2}, \tag{A3}$$

where

$$\begin{aligned}\Delta N&=\sqrt{\sum_{ij}\left(\frac{\partial N}{\partial Q(i,j)}\cdot\Delta Q\right)^2+\sum_{ij}\left(\frac{\partial N}{\partial I(i,j)}\cdot\Delta I\right)^2}\\&=\frac{\sqrt{(\Delta Q)^2\cdot\sum_{ij}I^2(i,j)+(\Delta I)^2\cdot\sum_{ij}Q^2(i,j)}}{\sum_{ij}I(i,j)},\end{aligned} \tag{A4}$$

$$\begin{aligned}\Delta D&=\sqrt{\sum_{ij}\left(\frac{\partial D}{\partial U(i,j)}\cdot\Delta U\right)^2+\sum_{ij}\left(\frac{\partial D}{\partial I(i,j)}\cdot\Delta I\right)^2}\\&=\frac{\sqrt{(\Delta U)^2\cdot\sum_{ij}I^2(i,j)+(\Delta I)^2\cdot\sum_{ij}U^2(i,j)}}{\sum_{ij}I(i,j)}.\end{aligned} \tag{A5}$$

Here ΔI, ΔQ, and ΔU indicate the rms noise of the Stokes I, Q, and U maps, respectively. Then, Equation (A3) can be expressed as

$$\Delta\langle\theta_{\rm Pol}\rangle_I=\frac{\sqrt{N^2\cdot(\Delta D)^2+D^2\cdot(\Delta N)^2}}{2(N^2+D^2)}. \tag{A6}$$

The intensity-weighted method always makes sense when applied to point sources, but it may lead to misjudgment in

certain extended cases, as the position angle in the extended regions also significantly contributes to the estimation, despite having much lower density. For comparison, we also follow the approach discussed by Galametz et al. (2020) and average the position angle of polarization by weighting it with its uncertainty σ. The value of σ is calculated by error propagation and described as

$$\sigma(i,j) = \sqrt{\left(\frac{\partial\theta_{\rm Pol}(i,j)}{\partial Q(i,j)}\cdot\Delta Q\right)^2 + \left(\frac{\partial\theta_{\rm Pol}(i,j)}{\partial U(i,j)}\cdot\Delta U\right)^2}, \tag{A7}$$

where $\theta_{\rm Pol}(i,j) = 0.5\cdot\arctan(U(i,j)/Q(i,j))$, and the averaging position of polarization angle weighted by the uncertainty $\langle\theta_{\rm Pol}\rangle_\sigma$ is expressed by

$$\langle\theta_{\rm Pol}\rangle_\sigma = 0.5\cdot\arctan\left(\frac{K}{M}\right), \tag{A8}$$

where M and K are average values of Stokes Q and U weighted by the uncertainty of the polarization position angle:

$$M = \frac{\sum_{ij}(Q(i,j)/\sigma^2(i,j))}{\sum_{ij}(1/\sigma^2(i,j))}, \quad K = \frac{\sum_{ij}(U_i/\sigma^2(i,j))}{\sum_{ij}(1/\sigma^2(i,j))}. \tag{A9}$$

The error of uncertainty-weighted angle $\Delta\langle\theta_{\rm Pol}\rangle_\sigma$ is estimated by multiplying the internal uncertainty iu derived from error propagation by the square root of the reduced χ^2:

$$\Delta\langle\theta_{\rm Pol}\rangle_\sigma = iu\cdot\sqrt{\frac{\chi^2}{n-1}}, \tag{A10}$$

where n is the total number of pixels and

$$iu = \frac{1}{\sqrt{\sum_{ij}(1/\sigma^2(i,j))}}, \quad \chi^2 = \sum_{ij}\left(\frac{(\theta_{\rm Pol}(i,j) - \langle\theta_{\rm Pol}\rangle_\sigma)^2}{\sigma^2(i,j)}\right). \tag{A11}$$

Note that the weighted polarization angle $\langle\theta_{\rm Pol}\rangle$ should be rotated by 90° to infer the mean direction of the B-field $\langle\theta_B\rangle$. The B-field position angles weighted by intensity $\langle\theta_B\rangle_I$ and uncertainty $\langle\theta_B\rangle_\sigma$ are available in Table 3.

Appendix B
Outflow Parameters

In many cases (47 protostars), blue- and redshifted outflows can be clearly paired in a bipolar fashion. However, there are nine protostars that only have one clear outflow component, while the other either is very weak or overlaps with other emission from, e.g., other outflows. It should be mentioned that HOPS-373E, HOPS-398, and HOPS-402 do not exhibit clear outflows.

To estimate the outflow direction, we measure its position angle using the following steps (see Figure 6): First, we connect the source center with the edges of the redshifted/blueshifted outflow lobe, and then we take the bisector of the open angle as the redshifted/blueshifted outflow position angle. The outflow direction is determined by averaging the position angles of the redshifted and blueshifted components. The edges of the lobes are defined using the 5σ level of the emission. For the monopolar cases, we take the position angle of the clear lobe as the outflow direction. Uniformly, the radius from center to lobe edge is set to $R = 1000$ au, as most sources have clear outflows at this scale. The outflow position angle $\theta_{\rm Out}$ and its corresponding mean open angle $\Delta\theta_{\rm Out}$ for each source are listed in Tables 3 and 4.

We define the position angle for each of the outflow edges as $\theta_{\rm edge} = \arctan(y/x)$, where $x^2 + y^2 = R^2$. Assuming that x and y have an error of half beam size u_3, i.e., $\Delta x = \Delta y = u_3$, then the error of $\theta_{\rm edge}$ is estimated by error propagation:

$$\Delta\langle\theta_{\rm edge}\rangle = \frac{u_3}{\sqrt{x^2+y^2}} = \frac{u_3}{R}, \tag{B1}$$

which is related to the location of the source within the OMC region. For monopolar and bipolar outflows, there are two (one lobe) and four (two lobes) independent measurements; thus, the error of $\theta_{\rm Out}$ can be expressed:

$$\Delta\langle\theta_{\rm Out}\rangle = \frac{\Delta\langle\theta_{\rm edge}\rangle}{\sqrt{2}} = \frac{u_3}{\sqrt{2}R}, \tag{B2}$$

for the cases with one clear lobe, and

$$\Delta\langle\theta_{\rm Out}\rangle = \frac{\Delta\langle\theta_{\rm edge}\rangle}{2} = \frac{u_3}{2R}, \tag{B3}$$

for the cases with two clear lobes. The outflow contours and position angles are shown in Figures 7–11. Since OMC1N-4-5-W field do not have outflow detection, we only show its intensity (see Figure 12).

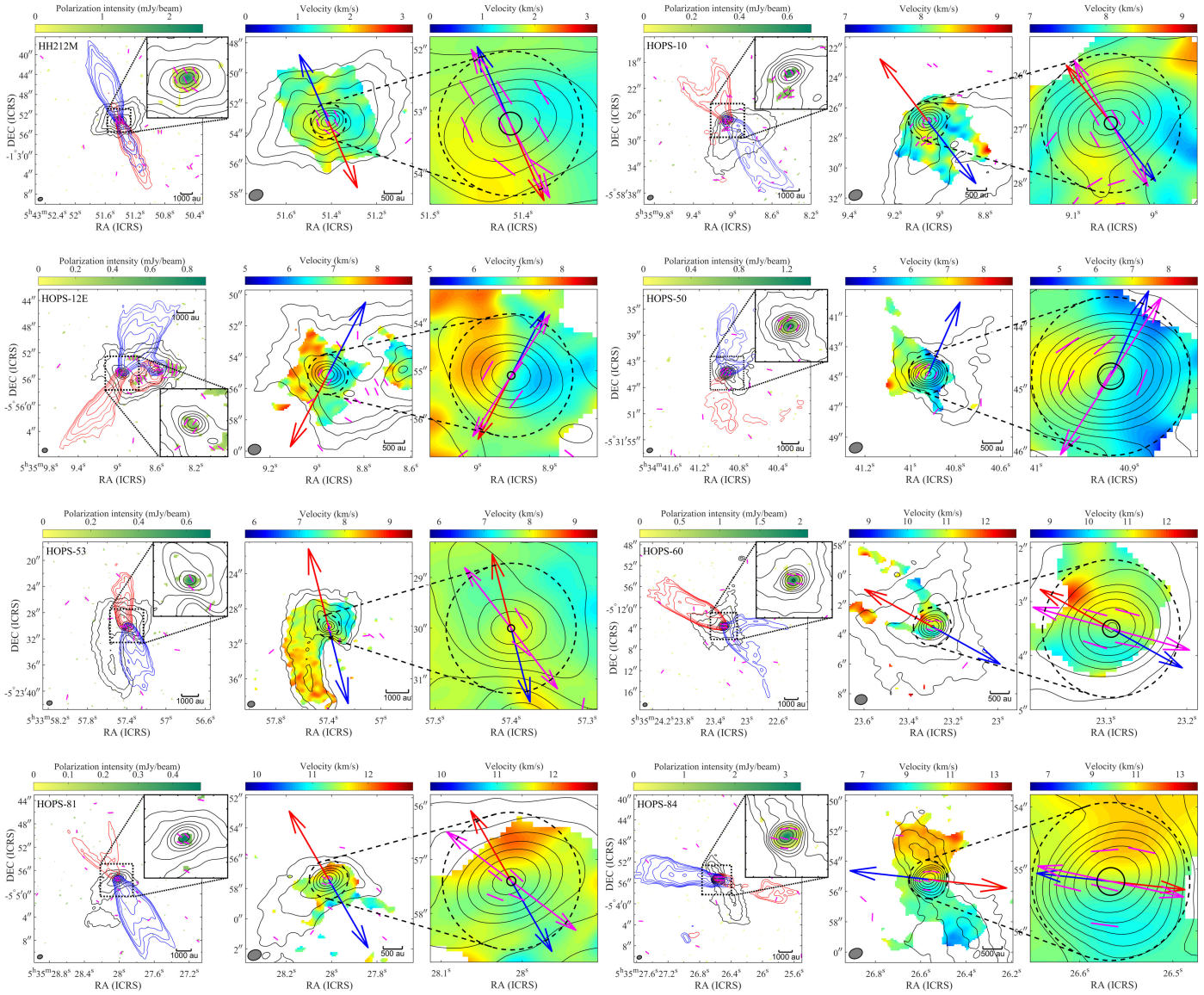

Figure 7. Self-scattering-dominated protostars. First column: 870 μm dust polarization intensity in color scale overlaid with redshifted and blueshifted outflow lobes (obtained from the ^{12}CO (3–2) line), the polarization segments, and the dust continuum emission (Stokes *I*) contours. Blue contours indicate the blueshifted outflow, while red contours indicate the redshifted outflow, with counter levels set at 5 times the outflow rms $\times$ (1, 2, 4, 8, 16, 32). The magenta segments represent the polarization. The regions of polarization intensity less than 3σ have been masked. Second column: the velocity field in color scale (obtained from the C^{17}O (3–2) line) overlaid with the polarization segments and Stokes *I* contours. Third column: an enlarged perspective of 1000 au of the second column. The magenta arrow indicates the mean polarization direction weighted by the intensity within the inner region of 400 au. In the second and third panels, the red and blue arrows indicate the mean direction of the redshifted and blueshifted outflows, respectively. For the velocity field, regions with an S/N less than 4 have been flagged. In all panels, the black contour levels for the Stokes *I* image are 10 times the rms $\times$ (1, 2, 4, 8, 16, 32, 64, 128, 256, 512). The black dotted square in the first column corresponds to a scale of 2000 au, while the black dashed circles correspond to a scales of 1000 au. The black solid circle indicates the disk size of the protostars, obtained from Tobin et al. (2020).

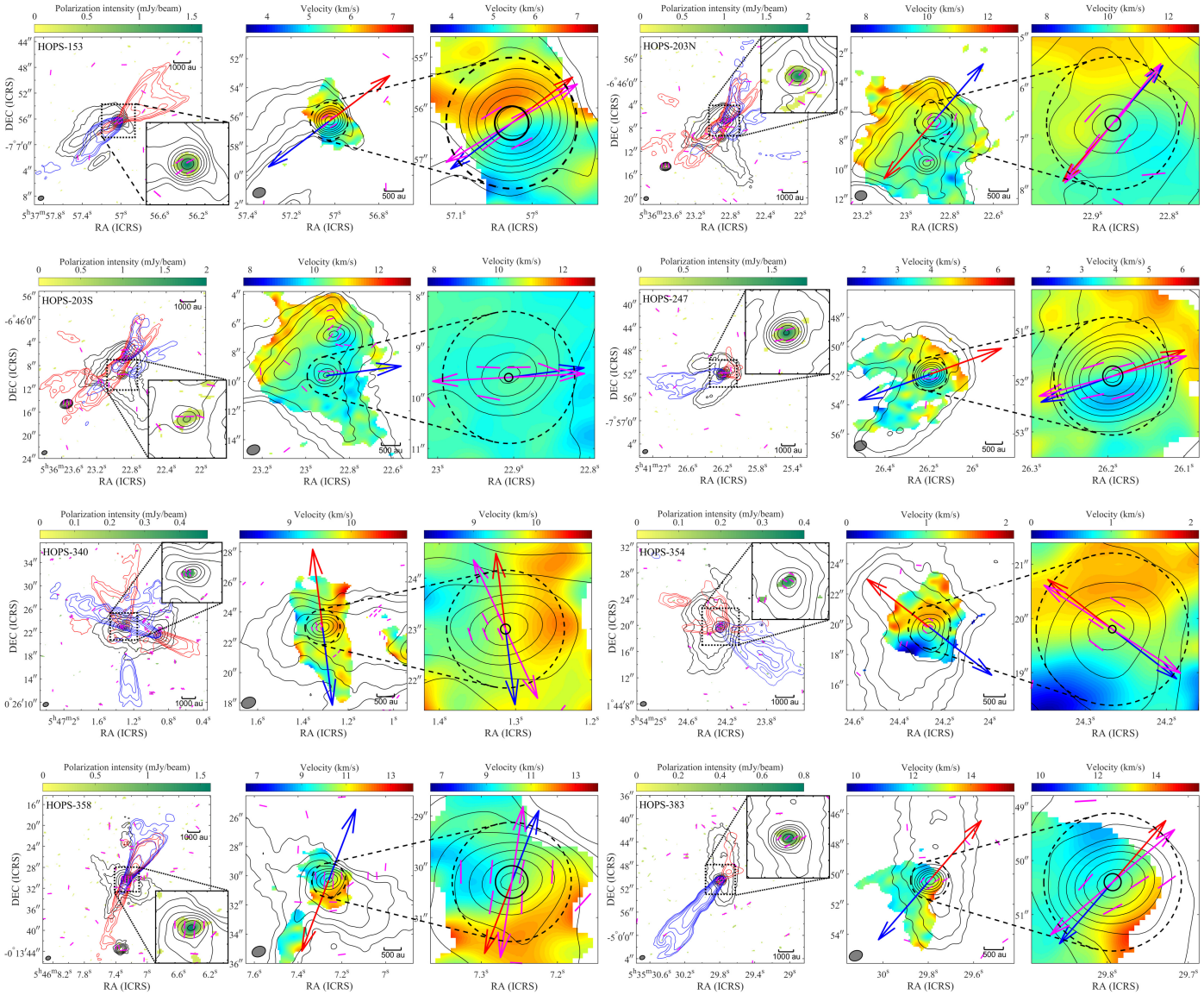

Figure 7. (Continued.)

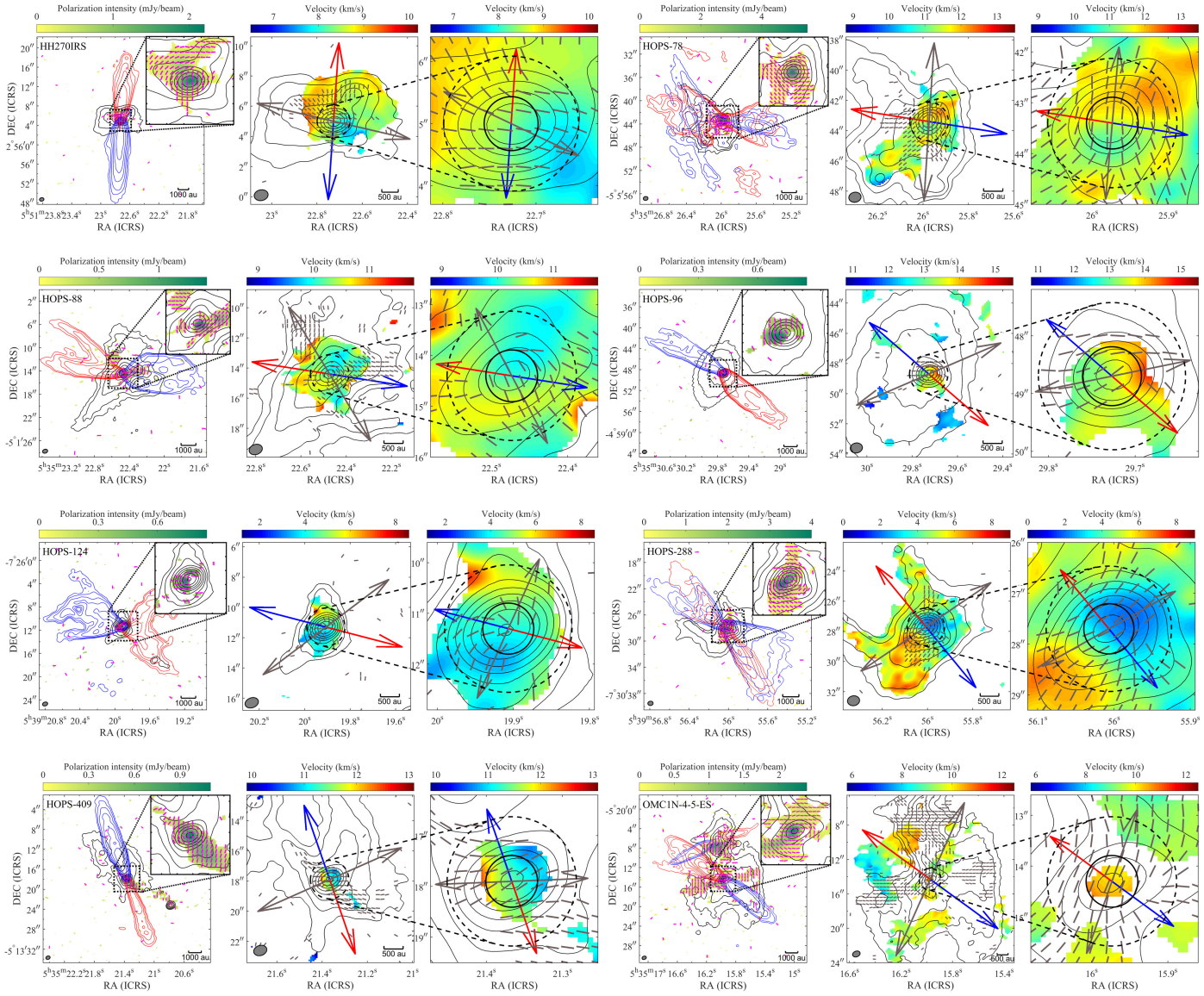

Figure 8. Perp-Type: velocity gradient direction $\perp$ outflow direction ($67.^{\circ}5 \leqslant |\theta_{\rm Out} - \theta_v| \leqslant 90^{\circ}$). First column: 870 μm dust polarization intensity in color scale overlaid with the redshifted and blueshifted outflow lobes (obtained from the ^{12}CO (3–2) line), polarization segments, and dust continuum emission (Stokes I) contours. Blue contours indicate the blueshifted outflow, while red contours indicate the redshifted outflow, with counter levels set at 5 times the outflow rms $\times$ (1, 2, 4, 8, 16, 32). The magenta segments represent the polarization. The regions of polarization intensity less than 3σ have been masked. Second column: the velocity field in color scale (obtained from the C^{17}O (3–2) line) overlaid with the B-field segments (i.e., polarization rotated by 90°) and Stokes I contours. Third column: an enlarged perspective of 1000 au of the second column. In the second and third panels, the black segments represent the B-fields. The red and blue arrows indicate the mean direction of the redshifted and blueshifted outflows, respectively. For the velocity field, regions with an S/N less than 4 have been flagged. The gray arrows in the second and third columns indicate the mean B-field directions weighted by the intensity including all the polarization segments and weighted by the uncertainty within an annular region of 400–1000 au, respectively. In all panels, the black contour levels for the Stokes I image are 10 times the rms $\times$ (1, 2, 4, 8, 16, 32, 64, 128, 256, 512). The black dotted square in the first column corresponds to a scale of 2000 au, while the black dashed and solid circles correspond to scales of 1000 and 400 au, respectively.

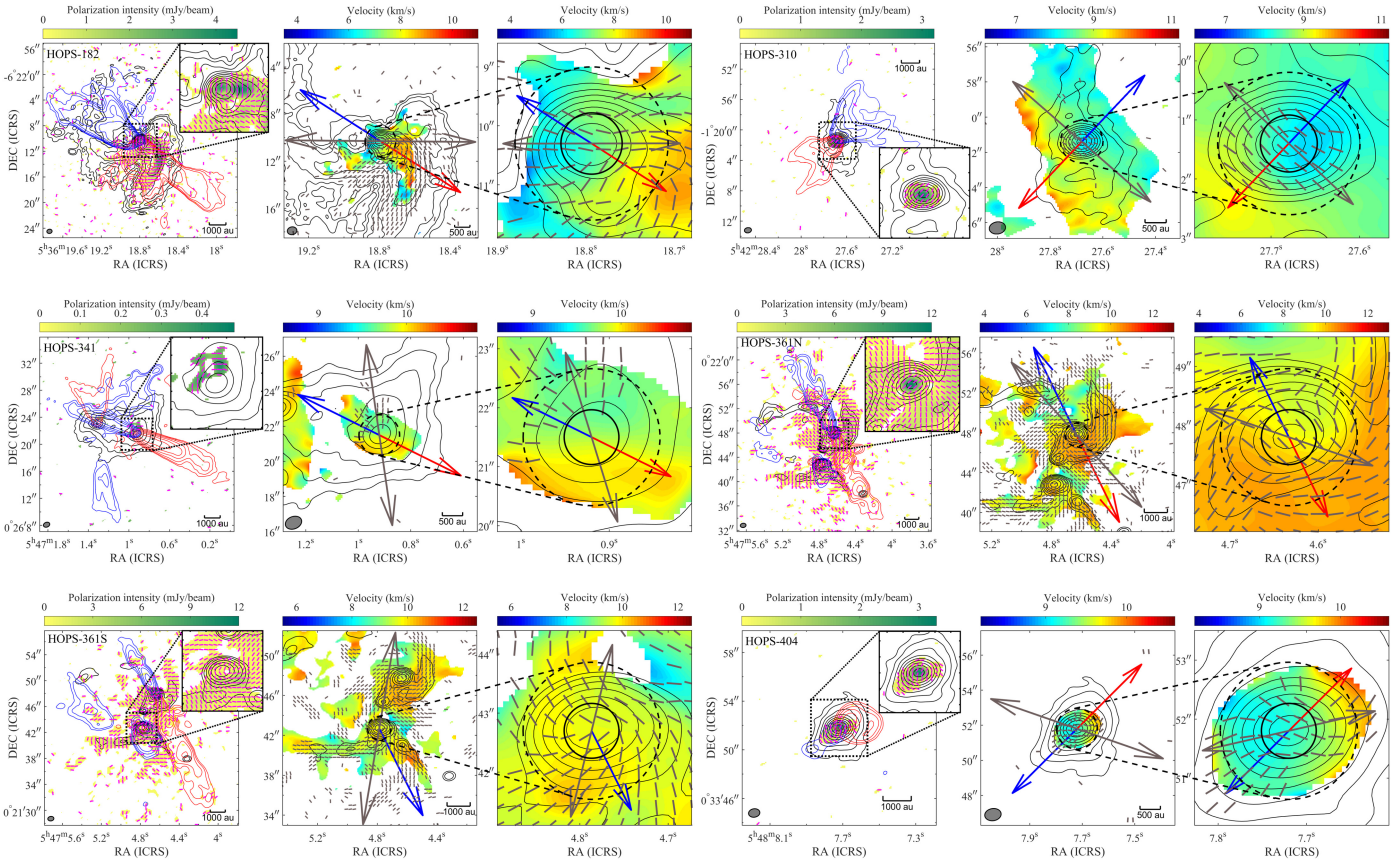

Figure 9. Nonperp-Type: velocity gradient direction is not perpendicular to outflow direction ($|\theta_{\rm Out} - \theta_v| < 67.^\circ5$). First column: 870 μm dust polarization intensity in color scale overlaid with the redshifted and blueshifted outflow lobes (obtained from the ^{12}CO (3–2) line), polarization segments, and dust continuum emission (Stokes *I*) contours. Blue contours indicate the blueshifted outflow, while red contours indicate the redshifted outflow, with counter levels set at 5 times the outflow rms × (1, 2, 4, 8, 16, 32). The magenta segments represent the polarization. The regions of polarization intensity less than 3σ have been masked. Second column: the velocity field in color scale (obtained from the C^{17}O (3–2) line) overlaid with the *B*-field segments (i.e., polarization rotated by 90°) and Stokes *I* contours. Third column: an enlarged perspective of 1000 au of the second column. In the second and third panels, the black segments represent the *B*-fields. The red and blue arrows indicate the mean direction of the redshifted and blueshifted outflows, respectively. For the velocity field, regions with an S/N less than 4 have been flagged. The gray arrows in the second and third columns indicate the mean *B*-field directions weighted by the intensity including all the polarization segments and weighted by the uncertainty within an annular region of 400–1000 au, respectively. In all panels, the black contour levels for the Stokes *I* image are 10 times the rms × (1, 2, 4, 8, 16, 32, 64, 128, 256, 512). The black dotted square in the first column corresponds to a scale of 2000 au, while the black dashed and solid circles correspond to scales of 1000 and 400 au, respectively.

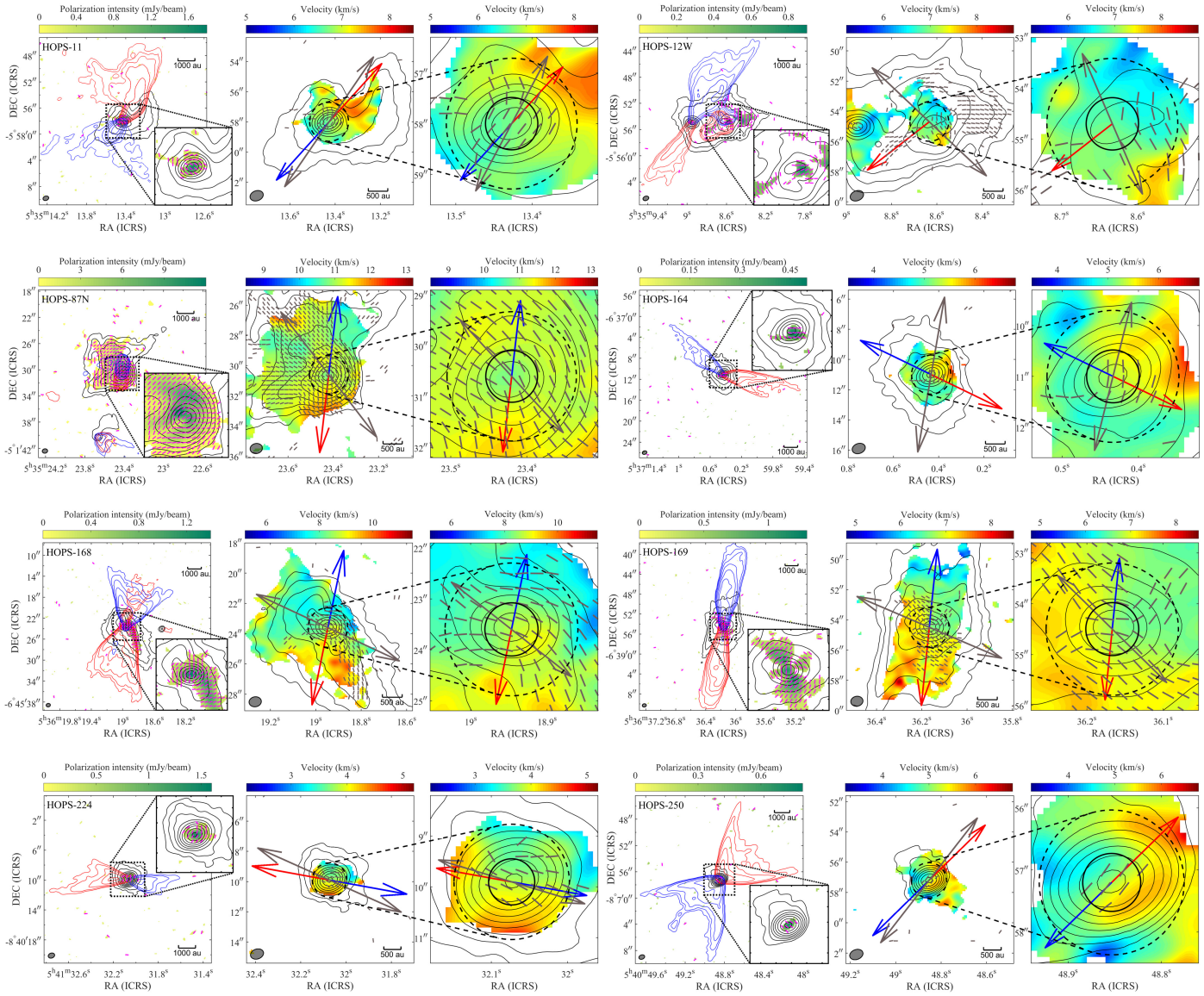

Figure 10. Unres-Type (26 including HOPS-250): velocity gradient is unresolved. First column: 870 μm dust polarization intensity in color scale overlaid with the redshifted and blueshifted outflow lobes (obtained from the ^{12}CO (3–2) line), polarization segments, and dust continuum emission (Stokes *I*) contours. Blue contours indicate the blueshifted outflow, while red contours indicate the redshifted outflow, with counter levels set at 5 times the outflow rms × (1, 2, 4, 8, 16, 32). The magenta segments represent the polarization. The regions of polarization intensity less than 3σ have been masked. Second column: the velocity field in color scale (obtained from the C^{17}O (3–2) line) overlaid with the *B*-field segments (i.e., polarization rotated by 90°) and Stokes *I* contours. Third column: an enlarged perspective of 1000 au of the second column. In the second and third panels, the black segments represent the *B*-fields. The red and blue arrows indicate the mean direction of the redshifted and blueshifted outflows, respectively. For the velocity field, regions with an S/N less than 4 have been flagged. The gray arrows in the second and third columns indicate the mean *B*-field directions weighted by the intensity including all the polarization segments and weighted by the uncertainty within an annular region of 400–1000 au, respectively. In all panels, the black contour levels for the Stokes *I* image are 10 times the rms × (1, 2, 4, 8, 16, 32, 64, 128, 256, 512). The black dotted square in the first column corresponds to a scale of 2000 au, while the black dashed and solid circles correspond to scales of 1000 and 400 au, respectively.

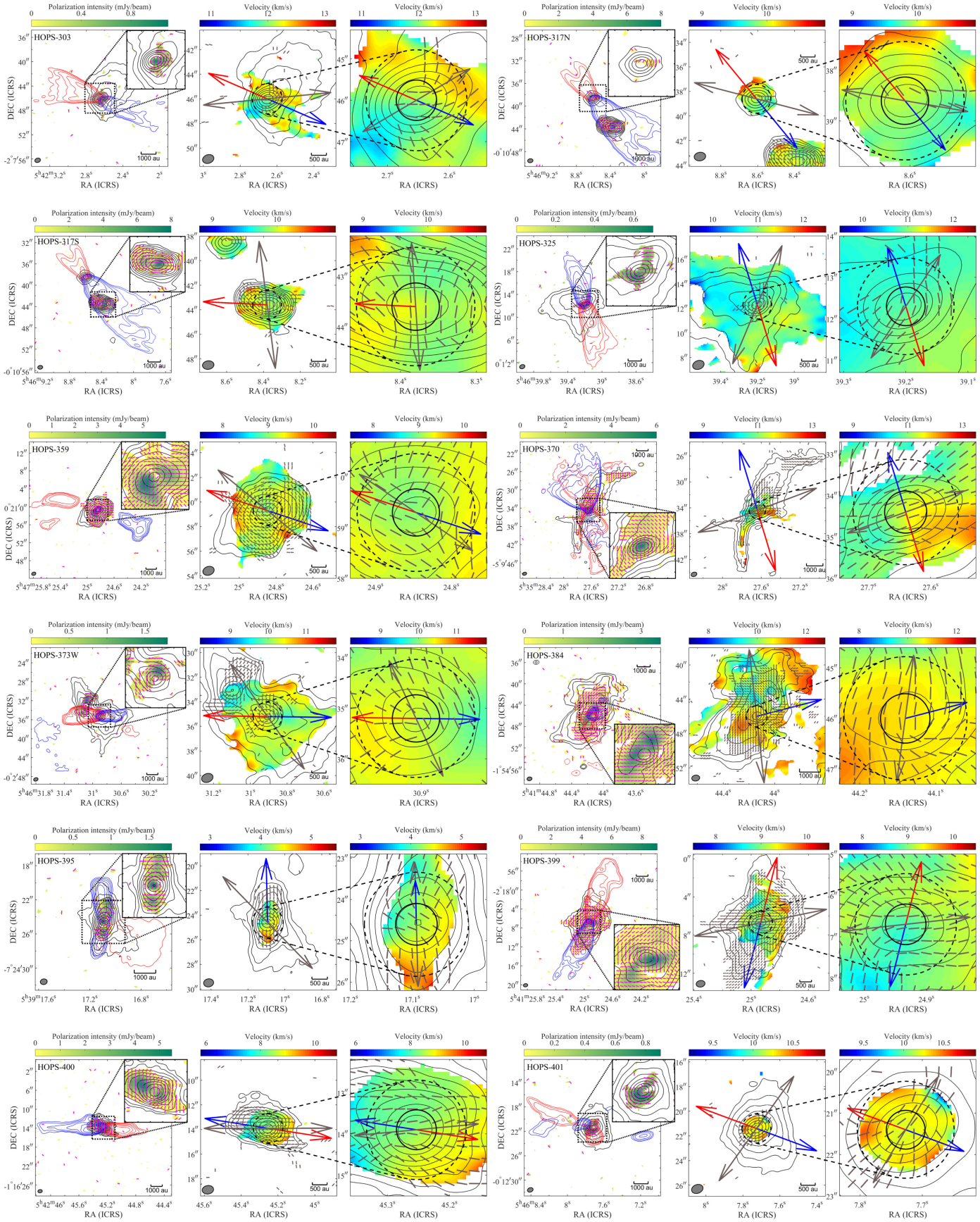

Figure 10. (Continued.)

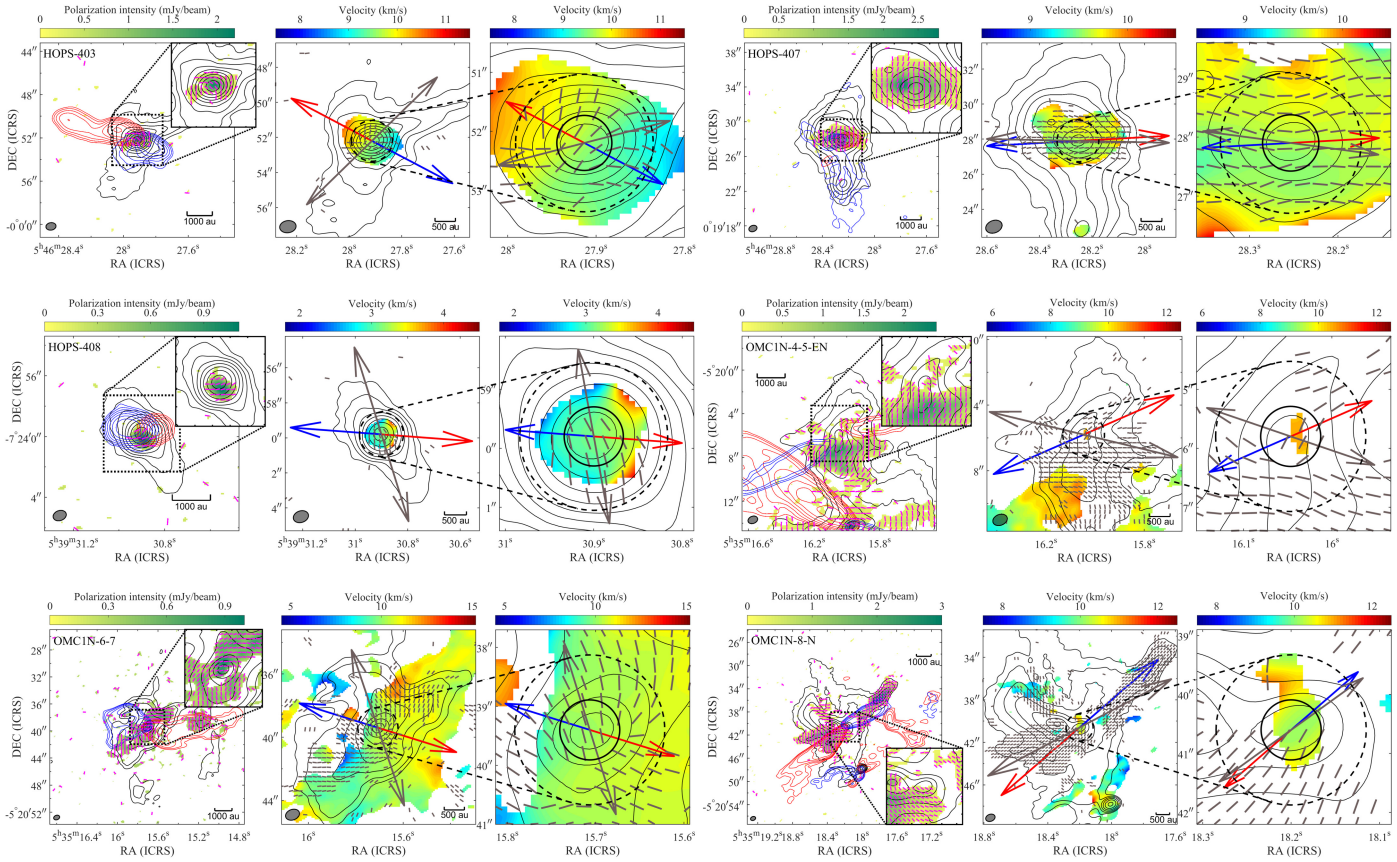

Figure 10. (Continued.)

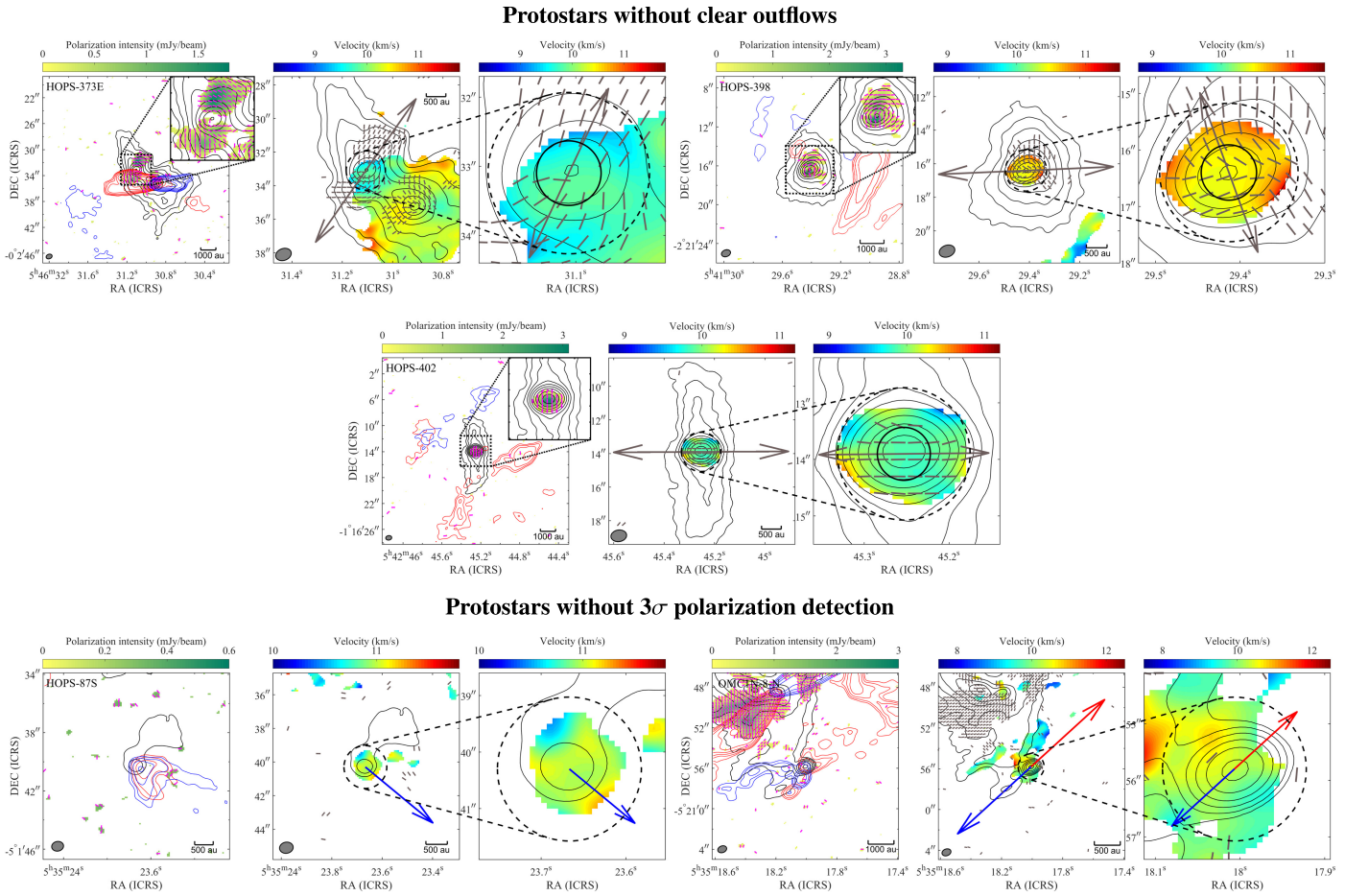

Figure 11. Other: protostars without clear outflows and without 3σ polarization detection. First column: 870 μm dust polarization intensity in color scale overlaid with the redshifted and blueshifted outflow lobes (obtained from the ^{12}CO (3–2) line), polarization segments, and dust continuum emission (Stokes *I*) contours. Blue contours indicate the blueshifted outflow, while red contours indicate the redshifted outflow, with counter levels set at 5 times the outflow rms $\times$ (1, 2, 4, 8, 16, 32). The magenta segments represent the polarization. The regions of polarization intensity less than 3σ have been masked. Second column: the velocity field in color scale (obtained from the C^{17}O (3–2) line) overlaid with the *B*-field segments (i.e., polarization rotated by 90°) and Stokes *I* contours. Third column: an enlarged perspective of 1000 au of the second column. In the second and third panels, the black segments represent the *B*-fields. The red and blue arrows indicate the mean direction of the redshifted and blueshifted outflows, respectively. For the velocity field, regions with an S/N less than 4 have been flagged. The gray arrows in the second and third columns indicate the mean *B*-field directions weighted by the intensity including all the polarization segments and weighted by the uncertainty within an annular region of 400–1000 au, respectively. In all panels, the black contour levels for the Stokes *I* image are 10 times the rms $\times$ (1, 2, 4, 8, 16, 32, 64, 128, 256, 512). The black dotted square in the first column corresponds to a scale of 2000 au, while the black dashed and solid circles correspond to scales of 1000 and 400 au, respectively.

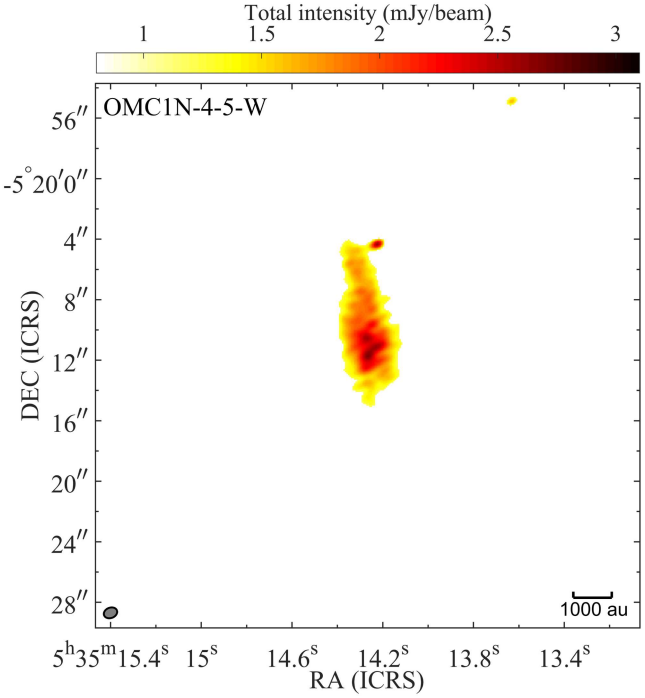

Figure 12. Starless core. Color scale indicates the total intensity.

Appendix C
$C^{17}O$ Opacity and Velocity Gradient

The opacity of $C^{17}O$ (3–2) is calculated by

$$\tau_\nu = -\ln\left(1 - \frac{T_R}{J_\nu(T_{\rm EX}) - J_\nu(T_{\rm cmb})}\right), \quad \text{(C1)}$$

where $T_{\rm cmb} = 2.722$ K is the cosmic microwave background temperature, and $J_\nu(T)$ is the Rayleigh–Jeans equivalent temperature of a blackbody at temperature T:

$$J_\nu(T)[\rm K] = \frac{h\nu}{k}\frac{[\rm m^2\ kg\ s^{-2}]}{[\rm m^2\ kg\ s^{-2}\ K^{-1}]} \cdot \frac{1}{e^{h\nu/kT} - 1}. \quad \text{(C2)}$$

Assuming that the Rayleigh–Jeans approximation is accurate, the observable source radiation temperature T_R is estimated as

$$T_R = 1222 \cdot \frac{I}{\nu^2 \theta_{\rm maj}\theta_{\rm min}} \cdot \frac{[\rm mJy\ beam^{-1}]}{[\rm GHz^2 \cdot arcsec^2]}, \quad \text{(C3)}$$

where $\theta_{\rm maj}$ and $\theta_{\rm min}$ are the major and minor axes of the restoring beam, respectively, and I is the peak of the $C^{17}O$ spectral line. The excitation temperature for an optically thick molecular line is estimated by

$$T_{\rm EX} = \frac{h\nu}{k} \cdot \ln\left(\frac{h\nu/k}{T_R + J_\nu(T_{\rm cmb})}\right). \quad \text{(C4)}$$

We have ^{12}CO detection, which is usually optically thick in the OMCs (e.g., Shimajiri et al. 2013; Eisner et al. 2016). $T_{\rm EX}(^{12}CO)$ ranges from 15.3 to 50.4 K at envelope scales of 400 au. Assuming $T_{\rm EX}(C^{17}O) \approx 50$ K, we then obtained the opacity of $C^{17}O$ for each source, with a range of 0.04–0.26, which is considered to be optically thin.

We estimate the velocity gradient by fitting the following function (Goodman et al. 1993; Tobin et al. 2011):

$$v_{\rm lsr} = v_\alpha \Delta\alpha + v_\delta \Delta\delta + v_0, \quad \text{(C5)}$$

where $\Delta\alpha$ and $\Delta\delta$ are the offsets in R.A. and decl., respectively, and v_α and v_δ are the projections of the velocity gradient onto the α and δ axes. The parameter v_0 represents the systemic velocity with respect to the local standard of rest. Then, the direction of velocity gradient θ_v is calculated by

$$\theta_v = \arctan(v_\delta / v_\alpha). \quad \text{(C6)}$$

The uncertainty is from a least-squares fit of Equation (C5) to the observed velocity field.

ORCID iDs

Bo Huang (黄博) https://orcid.org/0000-0001-7393-8583
Josep M. Girart https://orcid.org/0000-0002-3829-5591
Ian W. Stephens https://orcid.org/0000-0003-3017-4418
Manuel Fernández López https://orcid.org/0000-0001-5811-0454
Hector G. Arce https://orcid.org/0000-0001-5653-7817
John M. Carpenter https://orcid.org/0000-0003-2251-0602
Paulo Cortes https://orcid.org/0000-0002-3583-780X
Erin G. Cox https://orcid.org/0000-0002-5216-8062
Rachel Friesen https://orcid.org/0000-0001-7594-8128
Valentin J. M. Le Gouellec https://orcid.org/0000-0002-5714-799X
Charles L. H. Hull https://orcid.org/0000-0002-8975-7573
Nicole Karnath https://orcid.org/0000-0003-3682-854X
Woojin Kwon https://orcid.org/0000-0003-4022-4132
Zhi-Yun Li https://orcid.org/0000-0002-7402-6487
Leslie W. Looney https://orcid.org/0000-0002-4540-6587
S. Thomas Megeath https://orcid.org/0000-0001-7629-3573
Philip C. Myers https://orcid.org/0000-0002-2885-1806
Jaime E. Pineda https://orcid.org/0000-0002-3972-1978
Sarah Sadavoy https://orcid.org/0000-0001-7474-6874
Álvaro Sánchez-Monge https://orcid.org/0000-0002-3078-9482
Patricio Sanhueza https://orcid.org/0000-0002-7125-7685
John J. Tobin https://orcid.org/0000-0002-6195-0152
Qizhou Zhang https://orcid.org/0000-0003-2384-6589
James M. Jackson https://orcid.org/0000-0002-3466-6164
Dominique Segura-Cox https://orcid.org/0000-0003-3172-6763

References

Allen, A., Li, Z.-Y., & Shu, F. H. 2003, ApJ, 599, 363
Alves, F. O., Cleeves, L. I., Girart, J. M., et al. 2020, ApJL, 904, L6
Alves, F. O., Girart, J. M., Padovani, M., et al. 2018, A&A, 616, A56
Andersson, B. G., Lazarian, A., & Vaillancourt, J. E. 2015, ARA&A, 53, 501
Arce-Tord, C., Louvet, F., Cortes, P. C., et al. 2020, A&A, 640, A111
Bacciotti, F., Girart, J. M., Padovani, M., et al. 2018, ApJL, 865, L12
Beltrán, M. T., Padovani, M., Girart, J. M., et al. 2019, A&A, 630, A54
Briggs, D. S. 1995, PhD thesis, New Mexico Institute of Mining and Technology
CASA Team, Bean, B., Bhatnagar, S., et al. 2022, PASP, 134, 114501
Ciolek, G. E., & Mouschovias, T. C. 1994, ApJ, 425, 142
Cortés, P. C., Sanhueza, P., Houde, M., et al. 2021, ApJ, 923, 204
Cox, E. G., Harris, R. J., Looney, L. W., et al. 2018, ApJ, 855, 92
Dapp, W. B., & Basu, S. 2010, A&A, 521, L56
Eisner, J. A., Bally, J. M., Ginsburg, A., & Sheehan, P. D. 2016, ApJ, 826, 16
Federman, S., Megeath, S. T., Tobin, J. J., et al. 2023, ApJ, 944, 49
Fernández-López, M., Girart, J. M., López-Vázquez, J. A., et al. 2023, ApJ, 956, 82

Furlan, E., Fischer, W., Ali, B., et al. 2016, ApJS, 224, 5
Galametz, M., Maury, A., Girart, J. M., et al. 2018, A&A, 616, A139
Galametz, M., Maury, A., Girart, J. M., et al. 2020, A&A, 644, A47
Galli, D., Lizano, S., Shu, F. H., & Allen, A. 2006, ApJ, 647, 374
Girart, J. M., Beltrán, M. T., Zhang, Q., Rao, R., & Estalella, R. 2009, Sci, 324, 1408
Girart, J. M., Crutcher, R. M., & Rao, R. 1999, ApJL, 525, L109
Girart, J. M., Fernández-López, M., Li, Z. Y., et al. 2018, ApJL, 856, L27
Girart, J. M., Frau, P., Zhang, Q., et al. 2013, ApJ, 772, 69
Girart, J. M., Rao, R., & Marrone, D. P. 2006, Sci, 313, 812
Goodman, A. A., Benson, P. J., Fuller, G. A., & Myers, P. C. 1993, ApJ, 406, 528
Hennebelle, P., Commerçon, B., Chabrier, G., & Marchand, P. 2016, ApJL, 830, L8
Hennebelle, P., Commerçon, B., Lee, Y.-N., & Charnoz, S. 2020, A&A, 635, A67
Hirano, S., & Machida, M. N. 2019, MNRAS, 485, 4667
Hoang, T., & Lazarian, A. 2009, ApJ, 697, 1316
Hull, C. L. H., Le Gouellec, V. J. M., Girart, J. M., Tobin, J. J., & Bourke, T. L. 2020, ApJ, 892, 152
Hull, C. L. H., & Plambeck, R. L. 2015, JAI, 4, 1550005
Hull, C. L. H., Plambeck, R. L., Bolatto, A. D., et al. 2013, ApJ, 768, 159
Hull, C. L. H., Plambeck, R. L., Kwon, W., et al. 2014, ApJS, 213, 13
Hull, C. L. H., Yang, H., Li, Z.-Y., et al. 2018, ApJ, 860, 82
Hull, C. L. H., & Zhang, Q. 2019, FrASS, 6, 3
Joos, M., Hennebelle, P., & Ciardi, A. 2012, A&A, 543, A128
Kataoka, A., Muto, T., Momose, M., Tsukagoshi, T., & Dullemond, C. P. 2016, ApJ, 820, 54
Kataoka, A., Muto, T., Momose, M., et al. 2015, ApJ, 809, 78
Kataoka, A., Tsukagoshi, T., Pohl, A., et al. 2017, ApJL, 844, L5
Kounkel, M., Hartmann, L., Loinard, L., et al. 2017, ApJ, 834, 142
Kwon, W., Stephens, I. W., Tobin, J. J., et al. 2019, ApJ, 879, 25
Lada, C. J., & Lada, E. A. 2003, ARA&A, 41, 57
Le Gouellec, V. J. M., Hull, C. L. H., Maury, A. J., et al. 2019, ApJ, 885, 106
Le Gouellec, V. J. M., Maury, A. J., Guillet, V., et al. 2020, A&A, 644, A11
Lee, C.-F., Li, Z.-Y., Ching, T.-C., Lai, S.-P., & Yang, H. 2018, ApJ, 854, 56
Li, Z.-Y., Krasnopolsky, R., & Shang, H. 2013, ApJ, 774, 82
Liu, Y., Takahashi, S., Machida, M., et al. 2023, arXiv:2312.13573
Machida, M. N., Hirano, S., & Kitta, H. 2020, MNRAS, 491, 2180
Machida, M. N., Inutsuka, S.-i., & Matsumoto, T. 2007, ApJ, 670, 1198
Maury, A., Hennebelle, P., & Girart, J. M. 2022, FrASS, 9, 949223
Maury, A. J., Girart, J. M., Zhang, Q., et al. 2018, MNRAS, 477, 2760
Myers, P. C., Basu, S., & Auddy, S. 2018, ApJ, 868, 51
Myers, P. C., Stephens, I. W., Auddy, S., et al. 2020, ApJ, 896, 163
Ohashi, S., Kataoka, A., Nagai, H., et al. 2018, ApJ, 864, 81
Pattle, K., Fissel, L., Tahani, M., Liu, T., & Ntormousi, E. 2023, in ASP Conf. Ser. 534, Protostars and Planets VII, ed. S. Inutsuka et al. (San Francisco, CA: ASP), 193
Pineda, J. E., Segura-Cox, D., Caselli, P., et al. 2020, NatAs, 4, 1158
Pudritz, R. E., & Ray, T. P. 2019, FrASS, 6, 54
Qiu, K., Zhang, Q., Menten, K. M., et al. 2014, ApJL, 794, L18
Sadavoy, S. I., Myers, P. C., Stephens, I. W., et al. 2018a, ApJ, 859, 165
Sadavoy, S. I., Myers, P. C., Stephens, I. W., et al. 2018b, ApJ, 869, 115
Sanhueza, P., Girart, J. M., Padovani, M., et al. 2021, ApJL, 915, L10
Shimajiri, Y., Sakai, T., Tsukagoshi, T., et al. 2013, ApJL, 774, L20
Soler, J. D., Ade, P. A. R., Angilè, F. E., et al. 2017, A&A, 603, A64
Stephens, I. W., Dunham, M. M., Myers, P. C., et al. 2017a, ApJ, 846, 16
Stephens, I. W., Yang, H., Li, Z.-Y., et al. 2017b, ApJ, 851, 55
Stutz, A., Tobin, J., Stanke, T., et al. 2013, in Protostars and Planets VI Posters, ed. H. Beuther, R. S. Klessen, C. P. Dullemond, & T. Henning (Tucson, AZ: Univ. of Arizona Press)
Tobin, J. J., Hartmann, L., Chiang, H.-F., et al. 2011, ApJ, 740, 45
Tobin, J. J., Sheehan, P. D., Megeath, S. T., et al. 2020, ApJ, 890, 130
Vaillancourt, J. E. 2006, PASP, 118, 1340
Wang, W., Väisälä, M. S., Shang, H., et al. 2022, ApJ, 928, 85
Yang, H., Li, Z.-Y., Looney, L., & Stephens, I. 2016a, MNRAS, 456, 2794
Yang, H., Li, Z.-Y., Looney, L. W., Girart, J. M., & Stephens, I. W. 2017, MNRAS, 472, 373
Yang, H., Li, Z.-Y., Looney, L. W., et al. 2016b, MNRAS, 460, 4109
Yang, H., Li, Z.-Y., Stephens, I. W., Kataoka, A., & Looney, L. 2019, MNRAS, 483, 2371
Zhang, Q., Qiu, K., Girart, J. M., et al. 2014, ApJ, 792, 116
Zhao, B., Caselli, P., Li, Z.-Y., et al. 2020, MNRAS, 492, 3375